An ice-rich flow origin for the banded terrain in the Hellas basin, Mars.

X. Diot[1, 2], M.R. El-Maarry[3], L. Guallini[3], F. Schlunegger[1], K.P. Norton[4], N. Thomas[2, 3], S. Sutton[5], P.M. Grindrod[6,7]

[1]Institut für Geologie Universität Bern, Baltzerstrasse 1-3 CH-3012 Berne, Switzerland.

[2]Center for Space and Habitability, Universität Bern, Sidlerstrasse 5 CH- 3012 Berne, Switzerland.

[3]Physikalisches Institut, Universität Bern, Sidlerstrasse 5 CH- 3012 Berne, Switzerland.

[4]School for Geography, Environment and Earth Science, Victoria University of Wellington, New Zealand.

[5]Lunar and Planetary Laboratory, University of Arizona, Tucson, Arizona, USA.

[6]Department of Earth and Planetary Sciences, Birkbeck, University of London, London, UK

[7]Centre for Planetary Sciences at UCL/Birkbeck, London, UK.

Corresponding author.

Xavier Diot

Institut für Geologie Universität Bern

Baltzerstrasse 1-3 CH-3012, Switzerland

E-mail address: xavier.diot@geo.unibe.ch

Number of figures: 16

Number of Table: 1

To be submitted to JGR

This article has been accepted for publication and undergone full peer review but has not been through the copyediting, typesetting, pagination and proofreading process which may lead to differences between this version and the Version of Record. Please cite this article as doi: 10.1002/2015JE004956

Abstract

The interior of Hellas Basin displays a complex landscape and a variety of geomorphological domains. One of these domains, the enigmatic banded terrain covers much of the northwestern part of the basin. We use high-resolution (CTX and HiRISE) Digital Terrain Models to show that most of the complex viscous flowing behavior exhibited by the banded terrain is controlled by topography and flow-like interactions between neighboring banded terrain. Furthermore, the interior of the basin hosts several landforms suggestive of the presence of near-surface ice, which include polygonal patterns with elongated pits, scalloped depressions, isolated mounds and collapse structures. We suggest that thermal contraction cracking and sublimation of near-surface ice are responsible for the formation and the development of most of the ice-related landforms documented in Hellas. The relatively pristine form, lack of superposed craters, and strong association with the banded terrain, suggest an Amazonian (<3 Ga) age of formation for these landforms. Finally, relatively high surface pressures (above the triple point of water) expected in Hellas and summer-time temperatures often exceeding the melting point of water ice suggest that the basin may have recorded relatively "temperate" climatic conditions compared to other places on Mars. Therefore, the potentially ice-rich banded terrain may have deformed with lower viscosity and stresses compared to other locations on Mars, which may account for its unique morphology.

Keywords: Mars; Remote sensing; Permafrost; Ice.

Highlights

- The banded terrain hosts a large diversity of ice-related landforms
- Topography and bands' interactions control the shaping of the bands
- Water ice is likely present in the entire near-surface of the banded terrain

1. Introduction

Water, in its liquid or solid form, is considered to have modified the surface of Mars at numerous times in its history. Ground ice is expected to be present in the martian middle and high latitudes [*Boynton et al.*, 2002a; *Feldman et al.*, 2004; *Mitrofanov et al.*, 2002; *Mellon et al.*, 2004, 2009; *Dundas et al.*, 2014]. The Mars Odyssey Neutron Spectrometer and the Gamma Ray Spectrometer data have confirmed the presence of water ice in the near subsurface (first tens of cms) in high and mid latitudes [*Boynton et al.*, 2002b; *Prettyman et al.*, 2004; *Feldman et al.*, 2008; *Mangold et al.*, 2004; *Mellon et al.*, 2014]. In addition, hard ice-rich materials were observed underlying a thin layer of soil in trenches excavated by the Phoenix lander [e.g. *Mellon et al.*, 2009]. The presence of ice in the subsurface is likely to have driven permafrost-related processes and ice-related flows contributing to the modification of the surface of Mars during the Amazonian period [*Squyres*, 1979; *Squyres and Carr*, 1986; *Mangold and Allemand*, 2001; *Milliken et al.*, 2003; *Head et al.*, 2005; *Marchant and Head*, 2007; *Lefort et al.*, 2009; *Levy et al.*, 2009; *Dundas and McEwen*, 2010; *Gallagher et al.*, 2010; *Séjourné et al.*, 2011, 2012; *Berman et al.*, 2009, 2015].

A variety of landforms related to the presence of martian permafrost have been mapped in the middle and high latitudes of both hemispheres. These include thermal contraction polygons [e.g. *Mellon et al.*, 1997; *Mangold*, 2005; *Morgenstern et al.*, 2007; *Levy et al.*, 2010; *Seibert and Kargel*, 2001; *Soare et al.*, 2014], fractured mounds [*Soare et al.*, 2005, 2013; *Dundas et al.*, 2008; *Dundas and McEwen*, 2010] and scalloped depressions [*Lefort et al.*, 2009, 2010; *Séjourné et al.*, 2011, 2012]. Of significance to our study, the terrains surrounding the Hellas basin display several structures related to the deformation of ice in the form of viscous flow features [*Squyres*, 1979; *Milliken et al.*, 2003; *Head et al.*, 2005; *Mangold et al.*, 2005; *Berman et al.*, 2009; *Lefort et al.*, 2009, 2010; *Levy et al.*, 2010; *Hubbard et al.*, 2011; *Souness et al.*, 2012; *Hartmann et al.*, 2014]. In addition, multiple ice-related features such as

polygons or scalloped depressions have been mapped in the Peneus and Amphitritres Paterae in the southern proximity of Hellas [e.g. *Mangold,* 2005; *Lefort et al.,* 2010]. All of these landforms suggest the presence of near-surface ice in the vicinity of the basin.

In this study we focus on the NW region of Hellas basin's interior, which hosts a possibly unique terrain type described as "banded terrain" [*Thomas et al.*, 2010; *El-Maarry et al.*, 2012a; *Diot et al.*, 2014]. This terrain displays an alternation of sinuous bands and inter-bands suggestive of viscous flow behavior [*Diot et al.*, 2014]. *Diot et al*. [2014] additionally identified a few putative permafrost-related features in their initial mapping of the banded terrain suggesting an ice-rich composition. Therefore, we aim in this paper to: (i) expand the mapping and the geomorphological investigation of the ice-related landforms in NW Hellas using recently-acquired images; and (ii) try to better understand the mechanisms of formation of the banded terrain through 3D analysis of high-resolution (CTX and HiRISE) Digital Terrain Models (DTMs). In section 2, we describe the geological setting. In section 3, we provide information regarding the datasets and methods used and in section 4 we present our observations. Finally in section 5, we discuss the possible mechanisms of formation of the landforms and their implication regarding the geologic history of the region.

2. Geologic setting

Hellas basin (centered at 40°S, 68°E), situated in the southern mid-latitudes, is one of the oldest basins on Mars, with an age of ~4 Ga [*Werner,* 2008]. It is also one of the largest basins on Mars being more than ~3,000 km-long and ~1,500 km-wide [*Smith et al.*, 1999]. In addition, it hosts the deepest regions on the planet with depths greater than 7.5 km with respect to the reference elevation datum [*Smith et al.*, 1999]. Consequently, it is a major sink in the martian southern hemisphere for the deposition of sedimentary, volcanic or aeolian

material, as well as for the accumulation of liquid water or ice [e.g. *Cantor et al.*, 2001; *Bandfield et al.*, 2008; *Wilson et al.*, 2012].

The present-day surface of the basin appears relatively smooth compared to the surrounding highlands, probably because of post-impact modification of the landscape through fluvial, volcanic and glacial processes [e.g. *Leonard and Tanaka*, 2001; *Bernhardt et al.*, in press]. Indeed, the occurrence of a wide network of channels ending in the northwest of Hellas and the presence of fan deposits [*Moore and Howard*, 2005; *Wilson et al.*, 2010; *De Blasio*, 2014] suggest reworking by liquid-water flows in this part of the basin. Additionally, the northern and eastern flanks of the basin host young (late Amazonian) small viscous flow features [e.g. *Milliken et al.*, 2003; *Berman et al.*, 2009; *Head et al.*, 2005; *Hubbard et al.*, 2011; *Souness et al.*, 2012], and larger, older (Early Amazonian), lobate debris aprons that have been attributed to creep of ice-rich materials at the surface [e.g. *Squyres*, 1979; *Mangold and Allemand*, 2001; *Berman et al.*, 2009, 2015; *Levy et al.*, 2014].

Previous geomorphic and stratigraphic studies [e.g. *Tanaka and Leonard*, 1995; *Moore and Wilhelms*, 2001; *Diot et al.*, 2014; *Bernhardt et al.*, in press; *Berman et al.*, 2015] mapped several domains in the northwestern interior of the Hellas basin: the Alpheus Colles plateau, the honeycomb and polygonal ridge terrain (two domains named RT1 and RT2), the plain deposits (two depositions called P1 and P2) and the banded terrain. The major period of deposition in the interior of Hellas spans the period from the Late Noachian to the Amazonian [*Diot et al.*, 2014; *Bernhardt et al.*, in press]. One of these domains, the banded terrain is made up of juxtapositions of long and narrow (3–15 km-long, ~0.3 km-wide) sinuous and smooth bands frozen in the slope and has been suggested as evidence of viscous flow [*Diot et al.*, 2014].

Several geomorphologic landforms indicating the presence of near-surface ice [*Diot et al.*, 2014] have been locally observed in the banded terrain, which is the youngest domain of the interior of Hellas (Fig. 1). Among these landforms, two size groups (~10 m-wide and 20–60 m-wide) of thermal contraction polygons have been observed at the surface of the banded terrain. The small polygons are characterized by low centers and bulging edges, while the larger have high centers and bounding troughs [*Diot et al.*, 2014]. Furthermore, fractured mounds have been sporadically observed in the banded terrain [*Diot et al.*, 2014], which can indicate the presence of ice-cores below the surface.

3. Datasets and methods

The mapping and investigation of the landforms in the study region (Fig. 1) was carried out using datasets from: (i) the Mars Orbiter Laser Altimeter (MOLA) [*Smith et al.*, 2001] onboard the Mars Global Surveyor, (ii) the Context Camera (CTX) [*Malin et al.*, 2007], and (iii) the High Resolution Imaging Science Experiment (HiRISE) [*McEwen et al.*, 2007], the latter two instruments being onboard on NASA's Mars Reconnaissance Orbiter. We used a gridded MOLA elevation map of the entire surface of Mars, with a horizontal resolution of ~463 m/pixel at the considered latitudes. MOLA topography was used as a background for our mapping. CTX typically obtains 30 km-wide and 40 km-long images with a resolution of ~6 m/pixel. The HiRISE camera has a lower spatial coverage, although it offers an ultra-high spatial resolution of 0.25–0.5 m/pixel. CTX and HiRISE were used to characterize the morphology and to map the diverse landforms. CTX and HiRISE images were also used to build high resolution DTMs.

The mapping of the different structures was performed in the JMARS GIS environment (http://jmars.asu.edu) [*Gorelick et al.*, 2003] using files of points, which have been exported afterwards to ArcGIS 10.1 (http://www.esri.com/software/arcgis) to construct the final map.

In total, five HiRISE DTMs were used in this study (Table 1). HiRISE stereo pairs were controlled to MOLA Precision Experiment Data Records (PEDRs), using procedures developed for SOCET SET (BAE Systems, Inc.) stereophotogrammetric software [*Kirk et al.*, 2008]. Elevation posts (horizontal pixel scale) are at 1 or 2 m, depending on the source stereo images' pixel scale, and have an estimated vertical precision of 10s of cm to <2 m [*Kirk et al.*, 2008]. HiRISE DTMs were used to quantify the volume and the relief of selected landforms described in section 4.5. We calculated the volume (V) using the following equation:

$$V=\Delta z \times A$$

where Δz is the thickness of the structure and A is the area of one pixel of the DTM. The relief is obtained as the elevation difference between the highest and the lowest points [e.g. *Ahnert*, 1984] within 70 m × 70 m and 80 m × 80 m sliding windows [e.g. *Grohmann and Riccomini*, 2009], which are dynamic cells moving horizontally on the DTMs, with an overlap of the edges of the sliding windows. In addition, we used these DTMs to compute the slope in ArcGIS 10.1 of some of the features described in the section 4. Finally, two CTX DTMs were used in this study for 3 dimensional visualizations (Table 1). These DTMs have spatial resolutions of 20 m/pixel and were made using standard methods involving the ISIS and BAE Systems SocetSet software [e.g. *Kirk et al.*, 2008; *Okubo*, 2010; *Grindrod et al.*, 2012].

4. Results

We have identified several features in the interior of Hellas, mainly in the banded terrain (Fig. 1) that we interpret to be landforms related to the presence of near-surface ice. We have categorized them as: polygons, isolated mounds, arcuate depressions, hummocky areas and elliptical to circular depressions. Among these structures, the polygons, isolated mounds or hummocky areas were previously observed in a limited number of places [*Diot et al.*, 2014]. However, using recent HiRISE and CTX images, we were able to expand these earlier observations by identifying, mapping and categorizing additional features. Moreover, the 3-dimensional views have provided additional information concerning the morphometry of the banded terrain. Below, we briefly discuss these observations.

4.1. Polygons and elongated pits

The surface of the banded terrain displays multiple polygonal patterns of fractures (Fig. 2) of different sizes. Finer-scale observations using HiRISE images show that some of the large polygons display a regular rectangular shape, while others are more hexagonal with relatively sinuous troughs. Most of the small polygons have a hexagonal regular pattern. These different morphologies reveal the complex physical properties of the surface of the banded terrain. Locally, small polygons appear embedded in larger polygonal patterns (Fig. 2). Such polygonal patterns are recognizable in the entire banded terrain (Fig. 1).

In some areas, we observe small circular or elongated pits that are aligned within the N–S oriented troughs of the large polygons (Fig. 2A). These pits are not observed in the E–W oriented troughs of the large polygons. Likewise, the pit chains are sometimes isolated within a band and not linked to polygons (Fig. 3). The pits are typically 10 m to 20 m-wide, 20 m to

100 m-long, and have a smooth and relative flat floor (Fig. 3C). Using the length of shadows in HiRISE images, we estimate pit depths ranging from 1 m to 5 m.

4.2. Isolated mounds

The surface of the banded terrain hosts multiple isolated circular mounds (Fig. 4). Among them, two types have been identified based on their morphologies: fractured (Figs. 4A and 4B) [*Diot et al.*, 2014] and flat-topped mounds (Fig. 4C).

The fractured mounds (Figs. 4A and 4B) have diameters and heights in the range 20 to 50 m and 2 to 8 m, respectively. They often display fractures without a distinct pattern on their rounded summit [*Diot et al.*, 2014]. These mounds are surrounded by polygons or hummocky areas. On the other hand, the flat-top mounds (Fig. 4C) are larger with a diameters and heights in the range 70 to 160 m and 4 to 8 m, respectively. The tops of these mounds appear flat with few randomly oriented cracks. Both types of mounds have steep slopes that dip between 10° and 25° (Fig. 5). Mounds are mainly located in the northeastern part of the banded terrain (Fig. 1).

4.3. Arcuate depressions

CTX and HiRISE images reveal the presence of large arcuate depressions (Fig. 1, Figs. 6A and 6B) and multiple smaller ones (Fig. 7). The general morphology of these structures is composed of rimless arcuate depressions with a shape that varies from circular to elongate. Individual depressions consist of a flat floor broken by a relatively steep south facing slope (Figs. 6A, 6B and 7). These depressions roughly fall within two size groups: large and small depressions.

The large arcuate depressions are 300–2,000 m-wide and their south facing floors display numerous small polygons (Figs. 6A and 6B) with widths between 5 and 15 m and gentle wall slopes of ~3°. These polygons have a relatively high-elevated center and bounding troughs (Fig. 6B). In addition to the polygons, the internal surfaces of the large arcuate depressions display multiple putative aeolian dunes or mega-ripples (Fig. 6A).

Small arcuate depressions (Fig. 7) are 40 m to 120 m-wide, and are concentrated in impact craters or in local topographic lows on the surface of the bands. Similar to large arcuate depressions, very small polygons (1 m to 5 m-wide) are observable on their floors. Interestingly, these small arcuate depressions are located at different elevations with respect to each other (Fig. 7). Additionally, similar to the large ones, the small arcuate depressions have a south facing orientation. Small and large arcuate depressions are mainly localized in the southwestern sector of the banded terrain (Fig. 1).

4.4. Hummocky areas

The floor of the northwestern interior part of Hellas displays patches of knobby textures, which are referred to as the hummocky areas (Figs. 1 and 8). These hummocky areas consist of blocks that are 10–50 m-wide, 10–80 m-long, and 1–3 m-high based on length of shadow measurements on HiRISE images and DTM analysis. The blocks are randomly orientated within a given hummocky area (Fig. 8A). Such blocky textures are common in the banded terrain. They occur as well-defined local zones (Fig. 8) or as domains at the margins of the bands of the banded terrain and are indicative of lateral degradation [*Diot et al.*, 2014; see Figures 14C and 15]. The hummocky areas are also identified in impact craters of the P1 and P2 domains (Fig. 1).

The surfaces of the bands around the hummocky areas have slopes in the range 4–7° (Fig. 8B). The interiors of the hummocky areas display multiple steep slopes between 10 and 20°, corresponding to the edges of the blocks and relatively gentle slopes around 2–3° between the blocks (Fig. 8B).

4.5. Elliptical to circular depressions

Elliptical (Figs. 9A and 9B; ~20 % of the structures) to circular (Figs. 10A, 10B and 12A; ~80% of the structures) depressions are observed specifically in the banded terrain (Figs. 9–12). The general morphology of these features is characterized by a trough, more or less sinuous, surrounding a central part that is slightly depressed with respect to the surrounding terrain (Figs. 9–12). A fissure can be observed sometimes inside the trough (Fig. 10B). The elliptical forms have lengths that range between 100 m and 950 m, and length-to-width ratios in the range of 1.5–20 whereas the diameter of the circular shapes ranges from 30 m to 220 m. Overall, the elliptical forms do not show a preferential orientation.

Both types of depressions have rimless and sinuous boundaries. The central areas have the same texture as the surrounding terrains (Figs. 9–12) and occasionally display cracks, which are sometimes organized into polygonal patterns (Figs. 9A and 11A). In addition, the structures appear to show different degrees of evolution (Fig. 11). Indeed, some elliptical to circular depressions exhibit: (i) a barely visible boundary and a central part at the same level as the surrounding terrain (Fig. 11A); (ii) others have a well-defined structure with a clear central part surrounded by a relatively circular trough (Fig. 11B); and (iii) some of these depressions are made up of uneven, sinuous boundaries and completely degraded hummocky central areas (Fig. 11C).

Overall, the slope of the sides of the troughs ranges from 10° to 32° (Fig. 12B). The relief and the volume extracted for the troughs are in the range 4–7 m (Fig. 12C) and 40,000–660,000 m^3 respectively.

4.6. Signs of viscous flow

The morphology of most of the banded terrain, in particular the linear and lobate ones, displays multiple smooth changes in direction [*Diot et al.*, 2014]. The 3D views obtained from CTX and HiRISE DTMs (Figs. 13A, 13B and 14) reveal that the morphology of some of the linear and lobate banded terrain is strongly controlled by the surrounding topography. As illustrated in Figs. 13A, 13B and 15, most of the linear (noted 'b' Fig. 13A and 'c' Figs. 13B and 15) and lobate structures (noted 'a' Fig. 13A, 'e' Fig. 13B) start at topographic highs, follow the main slope and finish at distinctive terminal points. It should be noted that the lobate banded terrain ('a' Fig. 13A) terminate in a concentric form as the topography flattens out. Furthermore, the linear feature ('c' in the Figs. 13B and 15) is situated in a ~13 km-long and ~1.5 km-wide valley. Likewise, multiple curved banded terrain appear frozen in the slope (see Fig. 13A). Such landforms could be the result of a slow gravitational sliding.

The interaction between neighboring banded terrain appears to have played a significant role in the shaping of each banded terrain. For instance in Fig. 13A, the changing in orientation of the lobate banded terrain (letter 'a') coincides with the meeting with the northern linear one (letter 'b'); both landforms evolve in a parallel way afterwards. Furthermore in Figs. 13 B and 15, the linear banded terrain shown with the letter 'c' terminate in a concentric form where it converges with the lobate feature represented by the letter 'e' in Fig. 13B. In this case, the downslope movement of the lobate banded terrain ('e' Fig. 13B) resulted in a circular twisting of the termination of the linear landform ('c' Fig. 13B).

Finally, the 3D-view of a HiRISE DTM reveals a unique ~5 km-long, ~1.2 km-wide lobate banded terrain located on a slope of ~6° toward the northeast (Fig. 14). This elongated lobate banded terrain displays five lobes, which are separated by narrow depressions (colored stars in Fig. 14) perpendicular to the slope. The elevation profile along this landform shows a convex topography and a clear front (e.g., profile AA' in Fig. 14).

5. Discussion

The high resolution (HiRISE) datasets reveal the presence of numerous landforms, potentially indicative of near-surface ice, in the interior of Hellas basin, particularly in the banded terrain. The surface of the banded terrain display five main features: (1) polygons with different sizes and elongated pits, (2) isolated mounds with a fractured rounded top or a flat top, (3) arcuate depressions, (4) hummocky areas, and (5) elliptical to circular depressions. In the following sections, we use these observations to discuss the processes that could have led to the formation of these landforms, and the possible presence of ice in the subsurface of the banded terrain.

5.1. Formation mechanisms of putative landforms related to the presence of near-surface ice.

The suite of landforms described in this study is consistent with the surface expression of the degradation of near-surface ice. The degradation processes are likely to have comprised thermal contraction, sublimation of ice, and freeze-thaw cycles.

For instance, thermal contraction associated with the process of sublimation of ice can lead to the formation of features similar to the elongated pits (Figs, 1, 2 and 3) mostly associated

with the polygon troughs [e.g. *Mangold*, 2005; *Lefort et al.*, 2009]. In this context, seasonal thermal variations can induce the cracking of the upper-surface of the ground, forming a pristine polygonal pattern [e.g. *Lachenbruch*, 1962; *French*, 1996; *Mellon*, 1997; *Mangold*, 2005; *Levy et al.*, 2010]. Afterwards, the cracks will act as pathway for the sublimation of the ice, thereby causing local widening in pits of the initial cracks [e.g. *Mangold*, 2005; *Lefort et al.*, 2009]. Thus, these features point to permafrost-related processes, which are comparable with those documented in Utopia Planitia [e.g. *Lefort et al.*, 2009; *Mangold*, 2005], the north polar cap [*Mattson et al.*, 2014], and Valles Marineris [*Crosta et al.*, 2014].

Regarding the polygonal patterns (Fig. 2), the different shapes of polygons varying from hexagonal to regular rectangles reflect the complex physical properties of the surface of the banded terrain. The hexagonal polygons suggest a formation of the cracks more or less simultaneously in an originally homogeneous surface [e.g. *Lachenbruch*, 1962; *French*, 1996; *Mangold*, 2005]. The regular rectangular forms of certain large polygons could indicate a formation due to an anisotropic stress field leading to a slower sequential formation of fractures [e.g. *Lachenbruch*, 1962; *El-Maarry et al.*, 2010; 2012b]. Likewise, the spatial organization with the embedment of large and small polygons may imply two episodes during which the polygons were formed: (1) formation of the large high-center polygons, and (2) followed by the formation of the small low-center polygons, which overprint the larger ones. In addition, this arrangement can also indicate differences in ground penetration of the seasonal thermal wave leading to different propagation depths of cracks [e.g. *Mellon*, 1997; *Mangold*, 2005]. In this context, the large polygons may indicate a deeper propagation whereas the small polygons a shallower propagation of the cracks (e.g. *Lachenbruch*, 1961, 1962; *El-Maarry et al.*, 2010].

With respect to the isolated fractured and flat-topped mounds (Figs. 4 and 5), these landforms are morphologically and morphometrically analogous to other mounds observed on Mars,

particularly in Utopia Planitia. Production through the growth of ice lenses in the subsurface has been suggested for these ice-related features [e.g. *Soare et al.*, 2005, 2013; *Dundas et al.*, 2008; *Dundas and McEwen*, 2010]. Alternatively, the flat-topped mounds have a shape relatively similar to degraded remnants of impact craters [e.g. *Mangold*, 2003] also called ring-mold-craters [e.g. *Kress and Head*, 2008] observed on the surface of ice-related flows such as lobate debris aprons. These features have been interpreted to be the result of impacts into an ice-rich material followed by degradation via sublimation of ice [e.g. *Mangold*, 2003; *Kress and Head*, 2008]. Thus, despite different mechanism of formation, the two hypotheses proposed here suggest that the flat-topped mounds are indicative of the presence of near-surface ice.

The sublimation of ice-rich material may form structures analogous to the arcuate depressions (Figs. 6 and 7) and hummocky areas (Figs. 8A and 8B) observed in the banded terrain [e.g. *Mangold*, 2003; *Plescia et al.*, 2003; *Lefort et al.*, 2009, 2010; *Séjourné et al.*, 2011, 2012]. This process is known to create pitted surfaces [e.g. *Mangold*, 2003] or collapse structures [e.g. *Plescia et al.*, 2003; *Costard et al.*, 2008; *Lefort et al.*, 2009, 2010; *Séjourné et al.*, 2011] due to the vertical dissection of the terrain when the ice sublimates. Indeed, the arcuate depressions bear strong similarities, in terms of morphology and morphometry, to the smaller scalloped depressions observed in Utopia Planitia, Deuteronilus Mensae and Peneus and Amphitrites Patera, the latter being located south of Hellas [e.g. *Costard et al.*, 2008; *Lefort et al.*, 2009, 2010; *Séjourné et al.*, 2011, 2012). *Lefort et al.* [2009] suggested a formation via sublimation of an ice-rich material within hummocky terrains. More recently, the modeling work performed by *Dundas et al.* [2015] has shown that sublimation of near-surface excess ice may form the landforms analogous to the scalloped depressions without the need for melting. Furthermore, the hummocky areas are morphologically similar to other ice sublimation-related textures in the mid-latitudes including the "brain terrain" [*Levy et al.*,

2009], the "pit-and-butte" texture [*Mangold*, 2003] or the "brain-coral terrain" [*Noe Dobrea et al.*, 2007].

With regards to elliptical to circular depressions (Figs. 9–12), we tentatively favor a formation mechanism based on thermal contraction combined with the sublimation of ground ice (Fig. 16). The thermal contraction may form an initial circular fracture (red line on stage 1 in Fig. 16). The subsequent sublimation (e.g., blue arrows on stage 2 in Fig. 16) would proceed along the fracture, causing its widening. Progressive degradation of the initial fracture could then form the trough surrounding the central slightly depressed part (stage 3 in Fig. 16) observed on the HiRISE images (Figs. 9–12). The final stage is the complete degradation of the central part into a hummocky structure (Fig. 11C and stage 4 in Fig. 16). In this context, the volume (40,000–660,000 m^3) of the trough estimated may indicate to the volume of sublimated ice. Accordingly, the relief (4–7 m) may reflect the depth of the action of the sublimation process. The fact that these structures are isolated in the bands indicates a formation governed by local, rather than regional, stresses. However, an alternative possible origin for these structures is a formation due to thermokarst processes (i.e., through thawing of permafrost). Indeed, the elliptical to circular depressions share some similarities with Amazonian thermokarsts documented in the Danielson crater in the Arabia Terra region [e.g. *Baioni et al.*, 2014]. Nevertheless, unlike the case for thermokarst, we do not observe outflow channels [*Baioni and Sgavetti*, 2013; *Baioni et al.*, 2014] from the elliptical to circular depressions or any additional geomorphological evidence involving melting of ice.

5.2. Additional geomorphologic evidence of subsurface ice in the banded terrain

5.2.1. Geographic distribution and topographic control of ice-related structures

Our mapping reveals that the ice-related structures in Hellas are localized in the banded terrain (37°S–42°S) with local occurrences in impact craters in the terrains surrounding this domain (Fig. 1). Such landforms are generally constrained to the latitudinal band (35°–55° in both hemispheres) where permafrost-related landforms have been previously mapped on Mars [*Squyres and Carr*, 1986; *Head et al.*, 2003; *Mangold*, 2003; *Milliken et al.*, 2003]. This latitudinal dependence suggests a formation mainly controlled by climate [*Mellon and Jakosky*, 1993; *Head et al.*, 2003; *Lefort et al.*, 2009]. *Diot et al.* [2014] showed that the banded terrain is located in and along the rims of a trough [e.g. *Leonard and Tanaka*, 2001] in the northwest of the basin, which is the lowest elevated region on Mars.

Interestingly, the putative permafrost-related landforms are mostly (~80–90%) concentrated in the banded terrain, which suggest a close physical link between these features and the banded terrain. Furthermore, the suite of periglacial landforms extends laterally over the entire banded terrain. Consequently, their overall spatial extent may indicate the presence of ice in the entire near-surface of the banded terrain domain. A possible explanation for this is a preferential accumulation of ice in the region of the banded terrain, where the trough has acted as the ultimate base level. Further, *Diot et al.* [2014] suggested that the banded terrain have lost a significant amount of ice based on their concave topographic profiles and their multiple signs of weathering such as the progressive blocky degradations of some of the linear landforms. This assumption is supported by our new observations of ice-related landforms, particularly those of elliptical to circular depressions, which are evidence of strong degradation post-dating the emplacement of the banded terrain. However, the thickness of the ice remains poorly constrained. *Diot et al.* [2014] estimated a minimum

thickness of the banded terrain around 12 m, which incidentally is in the range of depths measured for the troughs of the elliptical to circular depressions. Taking into account that permafrost degradation operates on only the uppermost layer of the ground [e.g. *Mellon*, 1997; *Mangold*, 2005], we speculate that a thicker layer of ice may lie underneath the banded terrain.

5.2.2. Observation of a glacier-like form in the banded terrain and effect of the temperature on the deformation of the putatively ice-rich banded terrain.

The strong topographic control and the flow-like interactions between adjacent banded terrain are consistent with the complex viscous flow origin for the banded terrain proposed by *Diot et al.* [2014]. Indeed, interactions of neighboring landforms drive multiple changes in direction observed (Figs. 13A and 13B) with little evidence for brittle deformation. Moreover, the patches of convoluted banded terrain (white arrows in Fig. 13B) observed in some places between linear, lobate or concentric banded terrain can be the result of the deformation of unconsolidated material in response to convergence of adjacent banded terrain. However, no formation mechanism for these zones can be fully demonstrated at the time of the study and further investigations are required.

In addition, in the framework of an ice-flow as a mechanism of formation for the banded terrain, the unique lobate band terrain, displaying narrow depressions, (Fig. 14) may resemble a glacier-like form (GLF). The narrow depressions perpendicular to the main slope can be interpreted as analogous to terrestrial glacier crevasse-like fractures. In addition, the clear tongue shape, the convex topography and the well-defined front of the landform is analogous to the structure of the GLF [*Squyres*, 1979; *Milliken et al.*, 2003; *Head et al.*, 2005; *Hubbard et al., 2011*; *Souness et al.*, 2012; *Hartmann et al.*, 2014]. Due to the lack of information

concerning the underlying basal slope, we are not able to set the thickness of this lobate banded terrain. Further investigations, for instance using ground-penetrating radar data, are required to estimate the ice-thickness of this landform.

It is also worth noting that climate modeling [*Haberle et al.*, 2001; *Forget et al.*, 2013; *Wordsworth et al.*, 2013] shows that Hellas basin is one of the warmest places (maximum summer time temperature ~285 K) on Mars and has an atmospheric surface pressure of ~11.25 mbar [e.g. *Haberle et al.*, 2001], which is markedly above the triple point of water (~6 mbar). Accordingly Hellas has relatively "temperate" climatic conditions compared to other places on Mars. A consequence of this is that any deposits of ice could have been relatively warmer and deformed with lower viscosity and basal shear stresses [e.g. *Karlsson et al.*, 2015] than similar deposits elsewhere. This observation may account for the unique morphology and rheology of the linear and lobate banded terrain.

6. Conclusions

The analysis of CTX and HiRISE data sets reveals a variety of landforms indicative of near-surface ice in Hellas basin. Five main landforms have been documented: polygons, isolated mounds, arcuate depressions, hummocky areas and elliptical to circular depressions. Many of these structures occur in the banded terrain, which is also confined to the lowest region of Mars. Consequently, we suggest the presence of a strong genetic link between these ice-related landforms and the banded terrain.

The relatively fresh forms, the lack of craters, and the strong relationship between these features and the banded terrain suggest a recent formation during the Amazonian. The observed landforms are typical of the degradation of permafrost involving diverse

geomorphic processes and thus are markers of the presence of ice in the entire near-surface of the banded terrain. Thermal contraction cracking and sublimation of surface to near-surface ice are proposed as viable hypotheses of formation and development for most of the features described in the studied region.

The morphometric analysis of the troughs of the elliptical to circular depressions provides a relief between 4 and 7 m that may indicate the depth of the action of the sublimation process, i.e., the minimum thickness of the active ice layer. Furthermore, the volume (40,000–660,000 m^3) of ice sublimated from the collapse structures suggests a significant loss of ice of the banded terrain via reworking processes.

The analysis of the spatial organization of the banded terrain carried out in 3D views using CTX and HiRISE DTMs indicates that the morphology of most of the landforms is strongly linked to the surrounding topography and to the competition between adjacent banded terrain, which is consistent with a complex viscous flow in support of previous studies in the region. Finally, taking into account that the pressure in Hellas is above the triple point of water and that summer-time temperatures are relatively high compared to other locations on Mars, the basin may have recorded relatively "temperate" climatic conditions compared to other martian places. Thus, the ice deposits could have been warmer and would have deformed easily (with lower viscosity) compared to other ice-related flow features on Mars, which may account for the unique morphology and rheology of the banded terrain.

Acknowledgments

XD would like to thank the Center for Space and Habitability of the University of Bern for funding and supporting this study. LG, MR EL-M, NT, and FS are supported by funds from the Swiss National Science Foundation (SNSF). PMG is funded by the UK Space Agency (Aurora Fellowship grant ST/L00254X/1). The CTX stereo DTM processing was carried out at the UK NASA RPIF at University College London and the USGS guest photogrammetry facility. All the images used by this study are available to the public via the NASA's Planetary Data System (PDS) archive (https://pds.jpl.nasa.gov/). All the images can be accessed, viewed using the free JMARS (jmars.asu.edu) planetary Data System (PDS) archive. The authors would like to thank Romain Delunel for discussion and advices for the figures of the paper. The authors would like also to thank Hannes Bernhardt, Caleb Fassett and an anonymous reviewer for their constructive reviews, which improved the manuscript overall.

References

Ahnert, F., 1984. Local relief and the height limits of mountain ranges. American Journal of Science 284 (9), 1035–1055.

Baioni, D. and Sgavetti, M., 2013. Karst terrains as possible lithologic and stratigraphic markers in northern Sinus Meridiani, Mars. Planetary and Space Science 75(0), 173–181.

Baioni, D., Murana, A. and Tramontana, M., 2014. Amazonian thermokarst in Danielson crater, Arabia Terra region, Mars. Planetary and Space Science 104, Part B (0), 310–317.

Bandfield, J. L., 2008. High-silica deposits of an aqueous origin in western Hellas Basin, Mars. Geophysical Research Letters 35(12).

Berman, D. C., Crown, D. A. and Bleamaster, III, L.F., 2009. Degradation of mid–latitude craters on Mars. Icarus 200 (1), 77–95.

Berman, D. C., Crown D. A. and Joseph E.C., 2015. Formation and mantling ages of lobate debris aprons on Mars: Insights from categorized crater counts. Planetary and Space Science.

Bernhardt, H., Hiesinger, H., Ivanov, M. A., Ruesch, O., Erkeling, G. and Reiss, D., in press. Photogeologic mapping and the geologic history of the Hellas basin floor, Mars. Icarus 264, 407–442, doi:10.1016/j.icarus.2015.09.031.

Boynton, W., Feldman, W., Squyres, S., Prettyman, T., Brückner, J., Evans, L., Reedy, R., Starr, R., Arnold, J., Drake, D., Englert, P., Metzger, A., Mitrofanov, I., Trombka, J., dUston, C., Wänke, H., Gasnault, O., D.K., H., Janes, D., Marcialis, R., Maurice, S., S., Mikheeva, I., Taylor, G., Tokar, R. and Shinohara, C., 2002a. Distribution of Hydrogen in the Near Surface of Mars: Evidence for Subsurface Ice Deposits. Science 297, 81–85.

Boynton, W., Feldman, W., Mitrofanov, I. and Team, G., 2002b. Near-surface Ice on Mars: Early Results from the 2001 Mars Odyssey Gamma Ray Spectrometer (GRS) Instrument Suite. AGU Spring Meeting Abstracts, A7.

Cantor, B. A., James, P. B., Caplinger, M. and Wolff, M. J., 2001. Martian dust storms: 1999 Mars Orbiter Camera observations. Journal of Geophysical Research: Planets 106(E10), 23653–23687.

Costard, F., Forget, F., Madeleine, J. B., Soare, R. J. and Kargel, J. S., 2008. The origin and formation of scalloped terrain in Utopia planitia: insight from a general circulation model. Lunar and Planetary Science Conference, p. 1274.

Crosta, G. and De Blasio, F., 2014. Setting the Stage for a Model of Thermokarst Evolution of Valles Marineris, Mars. Lunar and Planetary Science Conference, pp. 2050.

De Blasio, F., 2014. Investigating the Hydrology of the Alleged Hellas Planitia Lake in Southern Mars. Lunar and Planetary Science Conference, pp. 1511.

Diot, X., El-Maarry, M., Schlunegger, F., Norton, K., Thomas, N. and Grindrod, P., 2014. The geomorphology and morphometry of the banded terrain in Hellas basin, Mars. Planetary and Space Science 101(0), 118–134.

Dundas, C. M. and McEwen, A. S., 2010. An assessment of evidence for pingos on Mars using HiRISE. Icarus 205(1), 244–258.

Dundas, C. M., Mellon M. T., McEwen A. S., Lefort A., Keszthelyi L. P. and Thomas N., 2008. HiRISE observations of fractured mounds: possible martian pingos. Geophysical Research Letters 35.

Dundas, C. M., Byrne, S. and McEwen, A., 2014. Clean Ground Ice on Mars: Evidence from Spacecraft, Fresh Craters, and Thermokarst. LPI Contributions 1791, 1375.

Dundas, C. M., Byrne, S. And McEwen, A. S., 2015. Modeling the development of martian thermokarst landforms. Icarus 262, 154–169.

El Maarry, M. R., W. J. Markiewicz, M. T. Mellon, W. Goetz, J. M. Dohm, and Pack A.,

2010. Crater floor polygons: desiccation patterns of ancient lakes on Mars? J. Geophys. Res., 115, E10006, doi:10.1029/2010JE003609.

El Maarry, M. R., Thomas, N. and Pommerol, A., 2012a. Banded Terrain and Associated Geology at the NW of Hellas Basin, Mars. Lunar and Planetary Science Conference, pp. 2653.

El Maarry, M. R., Kodikara, J., Wijessoriya, S., Markiewicz, W. J., and Thomas, N., 2012b. Desiccation mechanism for formation of giant polygons on Earth and intermediate-sized polygons on Mars: Results from a pre-fracture model, Earth and Planet. Sci. Lett. 323, 19–26.

Feldman, W. and Bourke, M., 2008. Estimate and Expression of Water Ice in Polar Sand Dunes. Planetary Dunes Workshop, pp. 33–34.

Feldman, W. C., Prettyman, T. H., Maurice, S., Plaut, J. J., Bish, D. L., Vaniman, D. T., Mellon, M. T., Metzger, A. E., Squyres, S. W., Karunatillake, S., Boynton, W. V., Elphic, R. C., Funsten, H. O., Lawrence, D. J. and Tokar, R. L., 2004. Global distribution of near-surface hydrogen on Mars. Journal of Geophysical Research: Planets 109(E9).

Forget, F., Wordsworth, R., Millour, E., Madeleine, J. B., Kerber, L., Leconte, J., Marcq, E., and Haberle, R. M., 2013. 3D modelling of the early martian climate under a denser CO2 atmosphere: temperatures and CO2 ice clouds. Icarus, 222(1), 81-99.

French, H. The Periglacial Environment, 1996. Addision Wesley Longman, Harlow.

Gallagher, C., Balme, M. R., Conway, S. J., and Grindrod, P. M., 2010. Sorted clastic stripes, lobes and associated gullies in high-latitude craters on Mars; landforms indicative of very recent, polycyclic ground-ice thaw and liquid flows, Icarus, 211, 458-471.

Gorelick, N., Weiss-Malik, M., Steinberg, B. and Anwar, S., 2003. JMARS: A Multimission Data Fusion Application. S. Mackwell and E. Stansbery, ed., Lunar and Planetary Science Conference, pp. 2057.

Grindrod, P. M., West, M., Warner,N. H., Gupta, S., 2012. Formation of an Hesperian-aged sedimentary basin containing phyllosilicates in Coprates Catena, Mars. Icarus, 218, 178-195, doi:10.1016/j.icarus.2011.11.027.

Grohmann, C. H. and Riccomini, C., 2009. Comparison of roving-window and search-window techniques for characterising landscape morphometry. Computers and Geosciences 35(10), 2164–2169.

Haberle, R. M., McKay, C. P., Schaeffer, J., Cabrol, N. A., Grin, E. A., Zent, A. P. and Quinn, R., 2001. On the possibility of liquid water on present-day Mars. Journal of Geophysical Research: Planets 106(E10), 23317–23326.

Hartmann, W. K., Ansan, V., Berman, D. C., Mangold, N. and Forget, F., 2014. Comprehensive analysis of glaciated martian crater Greg. Icarus 228(0), 96–120.

Head, J., Mustard, J. F., Kreslavsky, M., Milliken, R. E. and Marchant, D., 2003. Recent ice ages on Mars, 426, 797–802.

Head, J., Neukum, G., Jaumann, R., Hiesinger, H., Hauber, E., Carr, M., Masson, P., Foing, B., Hoffmann, H.; Kreslavsky, M., Werner, S., Milkovich, S., van Gasselt, S. and Team, H. C.-I., 2005. Tropical to mid-latitude snow and ice accumulation, flow and glaciation on Mars. Nature 434, 346-351.

Hubbard, B., Milliken, R. E., Kargel, J. S., Limaye, A. and Souness, C., 2011. Geomorphological characterisation and interpretation of a mid-latitude glacier-like form: Hellas Planitia, Mars. Icarus 211(1), 330–346.

Karlsson, N.B., Schmidt, L.S. and Hvidberg, C.S., 2015. Volume of martian midlatitude glaciers from radar observations and ice flow modeling. Geophysical Research Letters.

Kirk, R.L., Howington-Kraus, E., Rosiek, M.R., Anderson, J.A., Archinal, B.A., Becker, K. J., Cook, D.A., Galuszka, D.M., Geissler, P.E., Hare, T.M., Holmberg, I.M., Keszthe- lyi, L.P., Redding, B.L., Delamere, W.A., Gallagher, D., Chapel, J.D., Eliason, E.M., King, R.,

McEwen, A.S., 2008. Ultrahigh resolution topographic mapping of Mars with MRO HiRISE stereo images: meter-scale slopes of candidate Phoenix landing sites. Journal of Geophysical Research 113 (E3).

Kress, A.M. and Head, J.W., 2008. Ring-mold craters in lineated valley fill and lobate debris aprons on Mars: evidence of subsurface glacial ice. Geophysical Research Letters, 35.

Lachenbruch, A. H., 1961. Depth and spacing of tension cracks, J. Geophys. Res., 66(12), 4273–4292, doi:10.1029/JZ066i012p04273.

Lachenbruch, A. H., 1962. Mechanics of thermal contraction cracks and ice-wedge polygons in permafrost. Geological Society of America Special Papers 70, 1–66.

Lefort, A., Russell, P. S., Thomas, N., McEwen, A. S., Dundas, C. M. and Kirk, R. L., 2009. Observations of periglacial landforms in Utopia Planitia with the High Resolution Imaging Science Experiment (HiRISE). Journal of Geophysical Research: Planets 114(E4).

Lefort, A., Russell, P. and Thomas, N., 2010. Scalloped terrains in the Peneus and Amphitrites Paterae region of Mars as observed by HiRISE. Icarus 205(1), 259–268.

Leonard, G. J. and Tanaka, K. L., 2001. Geologic map of the Hellas region of Mars. U.S. Geological Survey Scientific Investigations Series Map I–2694, scale 1:5,000,000.

Levy, J. S., Head, J. W. and Marchant, D. R., 2009. Concentric crater fill in Utopia Planitia: History and interaction between glacial "brain terrain" and periglacial mantle processes. Icarus 202(2), 462–476.

Levy, J. S., Marchant, D. R. and Head, J. W., 2010. Thermal contraction crack polygons on Mars: A synthesis from HiRISE, Phoenix, and terrestrial analog studies. Icarus 206(1), 229–252.

Levy, J. S., Fassett, C.I, Head, J.W., Schwartz, C. and Watters, J.L., 2014. Sequestered glacial ice contribution to the global Martian water budget: geometric constraints on the volume of remnant, midlatitude debris-covered glaciers, Journal of Geophysical Research Planets, 119, 2188–2196, doi:10.1002/2014JE004685.

Malin, M. C., Bell, J. F., Cantor, B. A., Caplinger, M. A., Calvin, W. M., Clancy, R. T., Edgett, K. S., Edwards, L., Haberle, R. M., James, P. B., Lee, S. W., Ravine, M. A., Thomas, P. C. and Wolff, M. J., 2007. Context Camera Investigation on board the Mars Reconnaissance Orbiter. Journal of Geophysical Research: Planets 112(E5).

Mangold, N., 2003. Geomorphic analysis of lobate debris aprons on Mars at Mars Orbiter Camera scale: Evidence for ice sublimation initiated by fractures. Journal of Geophysical Research: Planets 108(E4).

Mangold, N., 2005. High latitude patterned grounds on Mars: Classification, distribution and climatic control. Icarus 174(2), 336–359.

Mangold, N. and Allemand, P., 2001. Topographic analysis of features related to ice on Mars. Geophysical Research Letters 28(3), 407–410.

Mangold N., Maurice S., Feldman W. C., Costard F., Forget F., 2004. Spatial relationships between patterned ground and ground ice detected by the neutron spectrometer on Mars. Journal of Geophysical Research 109.

Marchant, D. R. and Head., J.W., 2007. Antarctic dry valleys: Microclimate zonation, variable geomorphic processes, and implications for assessing climate change on Mars. Icarus 192(1), 187–222.

Mattson, S., Kilgallon, A., Byrne, S., McEwen, A., Herkenhoff, K., Okubo, C., Putzig, N. and Russell, P., 2014. Meter-Scale Pits in Mars North Polar Layered Deposits. Lunar and Planetary Science Conference, pp. 2431.

McEwen, A. S., Eliason, E. M., Bergstrom, J. W., Bridges, N. T., Hansen, C. J., Delamere, W. A., Grant, J. A., Gulick, V. C., Herkenhoff, K. E., Keszthelyi, L., Kirk, R. L., Mellon, M. T., Squyres, S. W., Thomas, N. and Weitz, C. M., 2007. Mars Reconnaissance Orbiters High Resolution Imaging Science Experiment (HiRISE). Journal of Geophysical

Research: Planets 112(E5).
Mellon, M. T., 1997. Small-scale polygonal features on Mars: Seasonal thermal contraction cracks in permafrost. Journal of Geophysical Research: Planets 102(E11), 25617–25628.
Mellon, M. T. and Jakosky, B. M., 1993. Geographic variations in the thermal and diffusive stability of ground ice on Mars. Journal of Geophysical Research: Planets 98(E2), 3345–3364.
Mellon, M. T., Feldman, W. C. and Prettyman, T. H., 2004. The presence and stability of ground ice in the southern hemisphere of Mars. Icarus 169(2), 324–340.
Mellon, M. T., Arvidson, R. E., Sizemore, H. G., Searls, M. L., Blaney, D. L., Cull, S., Hecht, M. H., Heet, T. L., Keller, H. U., Lemmon, M. T., Markiewicz, W. J., Ming, D. W., Morris, R. V., Pike, W. T. and Zent, A. P., 2009. Ground ice at the Phoenix Landing Site: Stability state and origin. Journal of Geophysical Research: Planets 114 (E1).
Mellon, M., Feldman, W., Hansen, C., Arvidson, R. and Sizemore, H., 2014. Ground-Ice Extremes in Martian Permafrost as Revealed by Periglacial Landforms. LPI Contributions 1791, 1106.
Milliken, R. E., Mustard, J. F. and Goldsby, D. L., 2003. Viscous flow features on the surface of Mars: observations from high–resolution Mars Orbiter Camera, (MOC) images. Journal of Geophysical Research: Planets 108 (E6).
Mitrofanov, I., Anfimov, D., Kozyrev, A., Litvak, M., Sanin, A., Tretyakov, V., Krylov, A., Shvetsov, V., Boynton, W., Shinohara, C., Hamara, D. and Saunders, R. S., 2002. Maps of Subsurface Hydrogen from the High Energy Neutron Detector, Mars Odyssey. Science 297(5578), 78–81.
Moore, J. M. and Wilhelms, D. E., 2001. Hellas as a possible site of ancient ice–covered lakes on Mars. Icarus 154 (2), 258–276.
Moore, J. M. and Howard, A. D., 2005. Large alluvial fans on Mars. Journal of Geophysical Research: Planets 110(E4).
Morgenstern A., hauber E., Reiss D., Van Gasselt S., Grosse G., Schirrmeister L., 2007. Deposition and degradation of a volatile-rich layer in Utopia planitia and implications for climate history on Mars. Journal of Geophysical Research 112.
Noe Dobrea, E., Asphaug, E., Grant, J., Kessler, M. and Mellon, M., 2007. Patterned Ground as an Alternative Explanation for the Formation of Brain Coral Textures in the Mid Latitudes of Mars: HiRISE Observations of Lineated Valley Fill Textures. LPI Contributions 1353, 3358.
Okubo, C. H., 2010. Structural geology of Amazonian-aged layered sedimentary deposits in southwest Candor Chasma, Mars. Icarus, 207, 210-225, doi:10.1016/j.icarus.2009.11.012.
Plescia, J., 2003. Amphitrites-Peneus Paterae/Malea Planum Geology. S. Mackwell and E. Stansbery, ed., Lunar and Planetary Science Conference, pp. 1478.
Prettyman, T. H., Feldman, W. C., Mellon, M. T., McKinney, G. W., Boynton, W. V., Karunatillake, S., Lawrence, D. J., Maurice, S., Metzger, A. E., Murphy, J. R., Squyres, S. W., Starr, R. D. and Tokar, R. L., 2004. Composition and structure of the Martian surface at high southern latitudes from neutron spectroscopy. Journal of Geophysical Research: Planets 109(E5).
Seibert N. M., Kargel J. S., 2001. Small-scale martian polygonal terrain; implication for liquid surface water. Geophysical Research Letters.
Séjourné, A., Costard, F., Gargani, J., Soare, R., Fedorov, A. and Marmo, C., 2011. Scalloped depressions and small-sized polygons in western Utopia Planitia, Mars: A new formation hypothesis. Planetary and Space Science 59, 412–422.
Séjourné, A., Costard F., Gargani J., Soare R.J. and Marmo C., 2012. Evidence of an eolian ice-rich and stratified permafrost in Utopia Planitia, Mars. Planetary and Space Science 60 (1), 248–254.

Smith, D. E., Zuber, M. T., Solomon, S. C., Phillips, R. J., Head, J. W., Garvin, J. B., Banerdt, W. B., Muhleman, D. O., Pettengill, G. H., Neumann, G. A., Lemoine, F. G., Abshire, J. B., Aharonson, O., David, C., Brown, Hauck, S. A., Ivanov, A. B., McGovern, P. J., Zwally, H. J. and Duxbury, T. C., 1999. The Global Topography of Mars and Implications for Surface Evolution. Science 284(5419), 1495–1503.

Smith, D. E., Zuber, M. T., Frey, H. V., Garvin, J. B., Head, J. W., Muhleman, D. O., Pettengill, G. H., Phillips, R. J., Solomon, S. C., Zwally, H. J., Banerdt, W. B., Duxbury, T. C., Golombek, M. P., Lemoine, F. G., Neumann, G. A., Rowlands, D. D., Aharonson, O., Ford, P. G., Ivanov, A. B., Johnson, C. L., McGovern, P. J., Abshire, J. B., Afzal, R. S. and Sun, X., 2001. Mars Orbiter Laser Altimeter: Experiment summary after the first year of global mapping of Mars. Journal of Geophysical Research: Planets 106(E10), 23689–23722.

Soare R., Burr D. and Wan Bun Tseung JM., 2005. Possible pingos and a periglacial landscape in northwest Utopia planitia. Icarus 174, 373–382.

Soare, R., Conway, S., Pearce, G., Dohm, J. and Grindrod, P., 2013. Possible crater-based pingos, paleolakes and periglacial landscapes at the high latitudes of Utopia Planitia, Mars. Icarus 225(2), 971–981.

Soare, R. J., Conway, S. J., and Dohm, J. M., 2014. Possible ice-wedge polygons and recent landscape modification by "wet" periglacial processes in and around the Argyre impact basin, Mars. Icarus 233: 214-228.

Souness, C., Hubbard, B., Milliken, R. E. and Quincey, D., 2012. An inventory and population–scale analysis of martian glacier–like forms. Icarus 217 (1), 243–255.

Squyres, S. W., 1979. The distribution of lobate debris aprons and similar flows on Mars. Journal of Geophysical Research: Solid Earth 84 (B14), 8087–8096.

Squyres, S. W. and Carr, M. H., 1986. Geomorphic Evidence for the Distribution of Ground Ice on Mars. Science 231(4735), 249–252.

Tanaka, K. L. and Leonard, G. J., 1995. Geology and landscape evolution of the Hellas region of Mars. Journal of Geophysical Research: Planets 100 (E3), 5407–5432.

Thomas, N., Beyer, R., Byrne, S., Moore, J. M., Wilson, S., Wray, J. J. and McEwen, A. S., 2010. The banded terrain in the NW region of Hellas basin. European Planetary Science Congress 2010, Abstract 338.

Werner, S., 2008. The early martian evolution constraints from basin formation ages. Icarus 195(1), 45–60.

Wilson, S. A., Moore, J. M., Howard, A. D., and Wilhelms, D. E., 2010. Evidence for ancient lakes in the Hellas region. Lakes on Mars. Elsevier BV, 195-222.

Wilson, S. A., Grant, J. A. and Howard, A. D., 2012. Distribution of intracrater alluvial fans and deltaic deposits in the southern highlands of Mars. Lunar and Planetary Science Conference, Abstract 2462.

Wordsworth, R., Forget, F., Millour, E., Head, J. W., Madeleine, J. B., and Charnay, B., 2013. Global modelling of the early martian climate under a denser CO2 atmosphere: water cycle and ice evolution. Icarus, 222(1), 1-19.

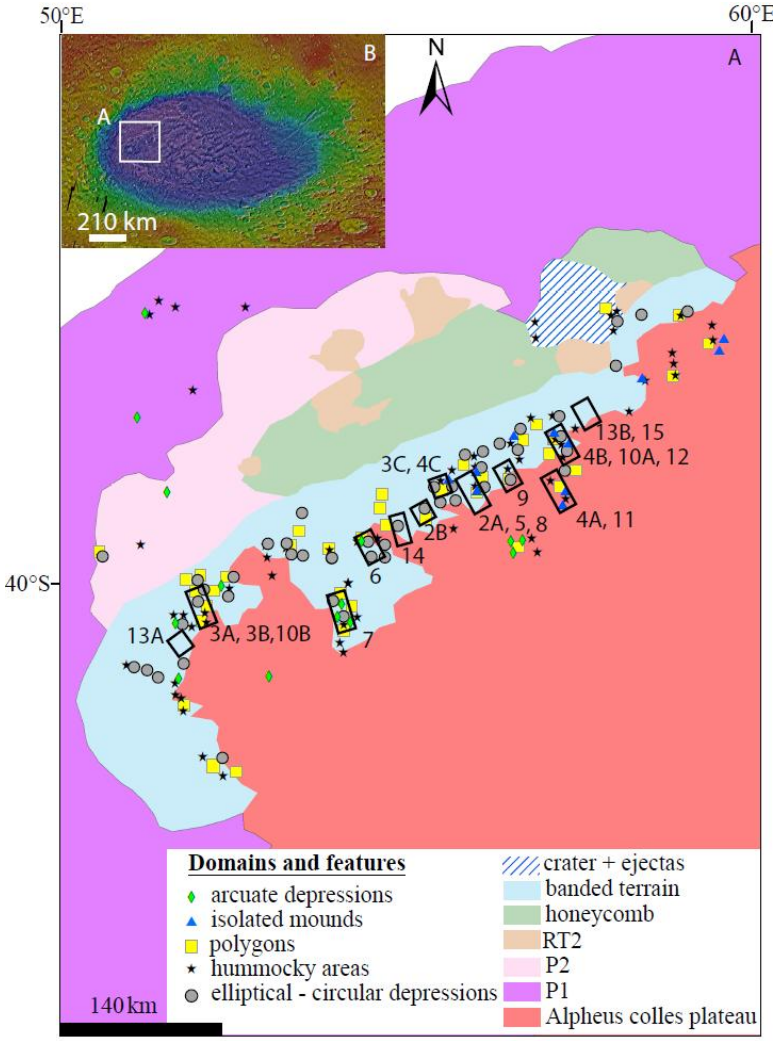

Figure 1. (A) *Geomorphologic map of the NW Hellas basin showing the different domains and the location of the ice-related landforms and (B) insight of a general THEMIS day IR map overlaid with MOLA color elevation map of Hellas to present the location of the study area (white box on the B). The colored areas on the map (A) represent the different domains and the color symbols show the landforms for clarity. Colored areas are: the Alpheus Colles plateau (red), a local crater with its ejecta (dashed blue), the plain deposit 1 (P1; dashed black), the plain deposit 2 (P2; pink), the honeycomb terrain (green), the reticulate terrain 2 (RT2; maroon), and the banded terrain (light blue). Colored symbols are: arcuate depressions (green diamonds), isolated mounds (blue triangles), polygons (yellow squares), hummocky areas (violet stars), and elliptical to circular depressions (red dots). The black boxes associated with black numbers indicate the location of the other figures of the paper.*

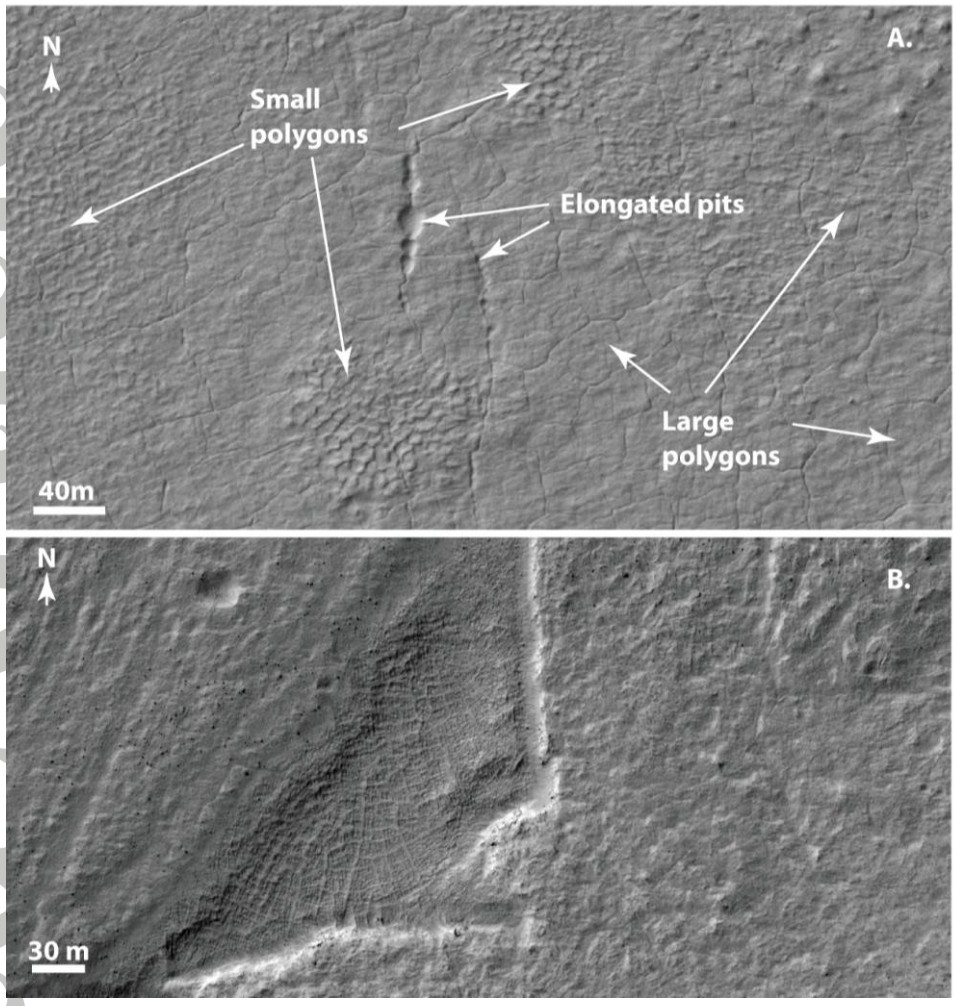

Figure 2. *Two examples of HiRISE views showing large and small polygons observed in the banded terrain. (A) Geometric relationships between small and large polygons observed at the surface of the bands. A chain of pits is clearly visible in an N–S oriented boundary of a polygon (image ID: PSP_007570_1415; image center: 38.2°S, 56.2°E). (B) Focus on a polygonal pattern observed at the surface of a banded terrain (image ID: PSP_006278_1410; image center: 38.8°S, 55.4°E).*

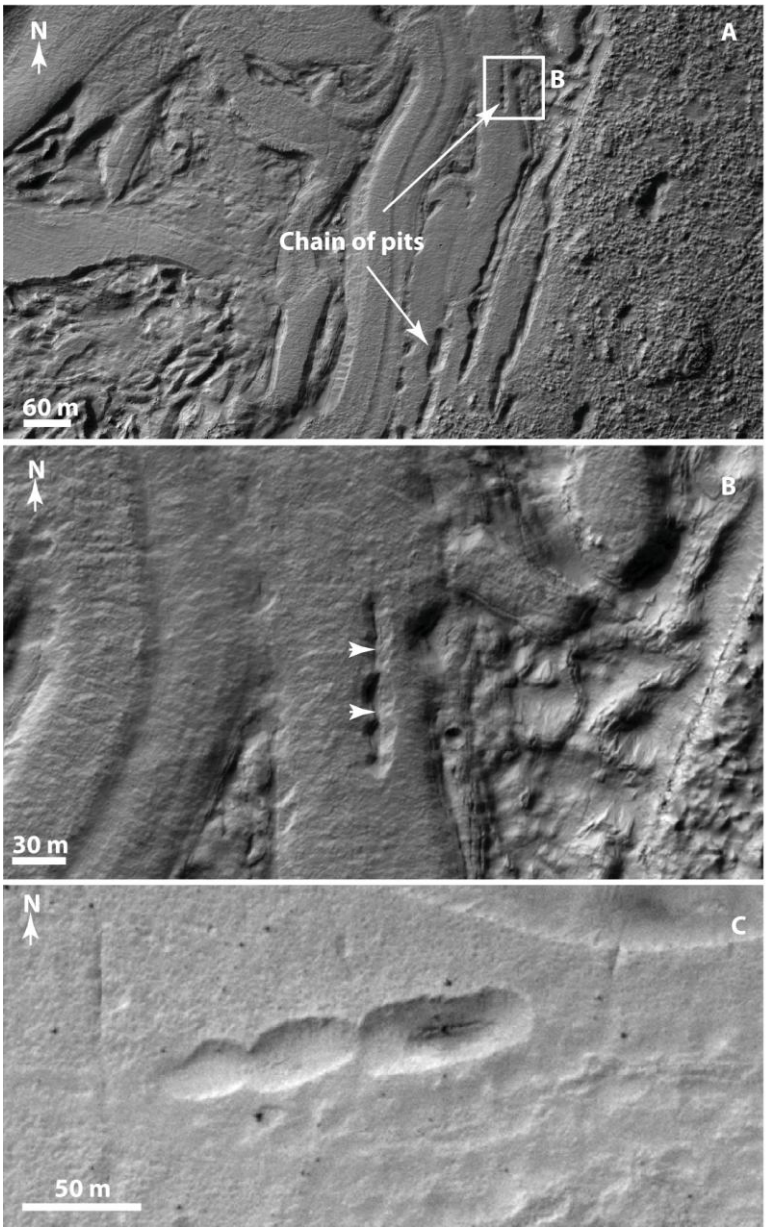

Figure 3. *Examples of pit chains observed by HiRISE on the surface of the banded terrain. (A) Two N-S oriented chains of pits located in the middle of a band (image ID: ESP_025635_1395; image center: 40.2°S, 52.2°E). (B) Close-up of a chain of pits indicated by the white box B in Fig. 3A (image ID: ESP_025635_1395; image center: 40.2°S, 52.2°E). On this close-up, we can easily see the relatively circular shape of the pits and the fracture on the bottom of them (white arrows). (C) This chain of pits is oriented E-W and is isolated in a band (image ID: ESP_033573_1420; image center: 37.9°S, 55.9°E). On this image, we can observe the relatively circular morphology of the pits and their flat floor.*

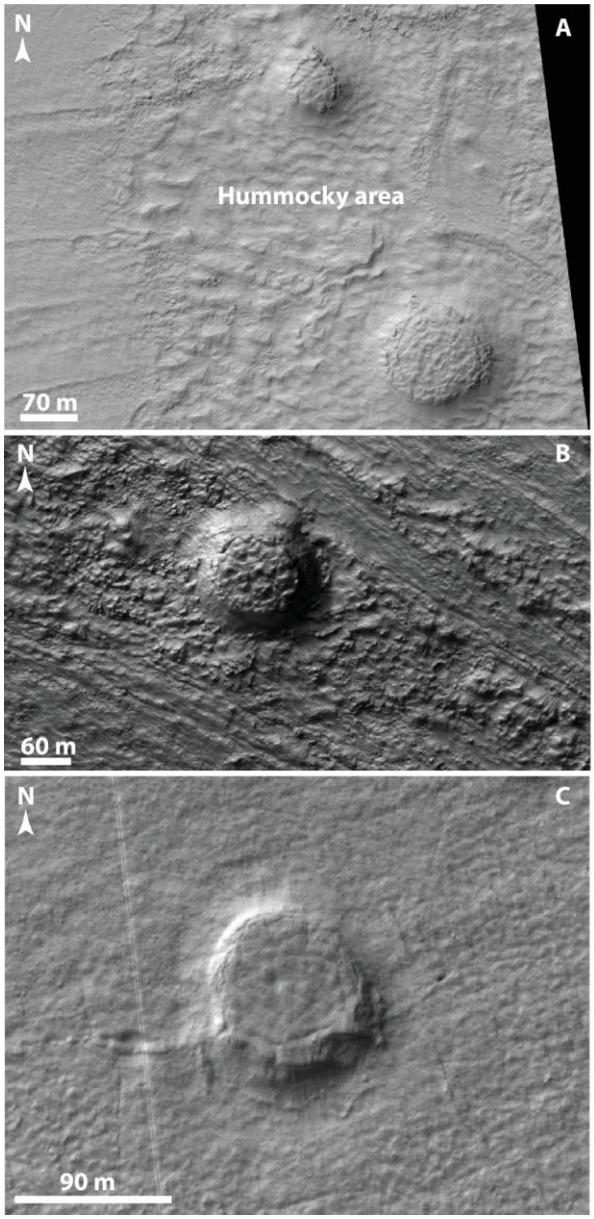

Figure 4. *HiRISE views of the both types of isolated mounds: fractured and flat-topped mounds. (A) Two fractured mounds surrounded by a hummocky area (image ID: PSP_006568_1415; image center: 38.3°S, 57.4°E). On this view, the mounds display a rounded top with fractures randomly oriented. (B) Fractured mound surrounded by a pitted surface (image ID: ESP_026360_ 1415; image center: 38°S, 57.4°E). The rounded top of this mound also displays randomly oriented fractures. (C) Typical flat-topped mounds recognizable at the surface of the bands (image ID: ESP_033573_1420; image center: 37.9°S, 55.9°E). This mound shows steep sides and very few fractures on its top.*

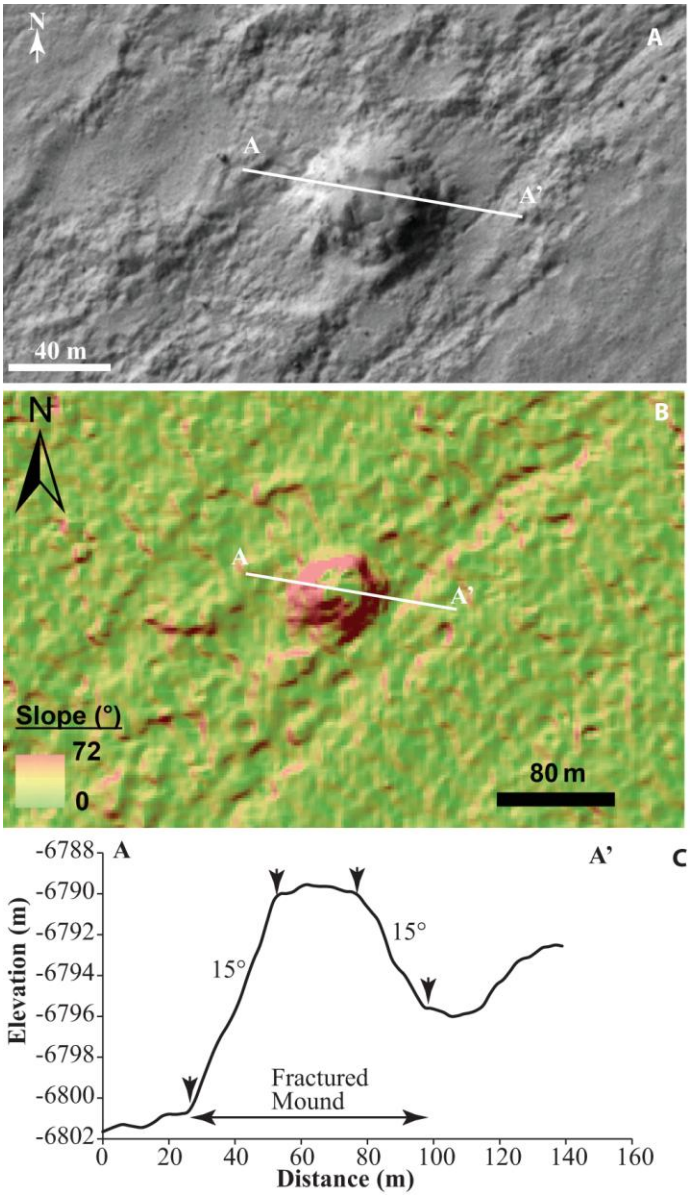

Figure 5. *HiRISE view and slope map from a HiRISE DTM (HiRISE DTM ID: DTEED_007570_1415_006779_1415) to quantify the steepness of the flanks of a typical fractured mound. (A) HiRISE observation of the given fractured mound surrounded by a hummocky area. The profile AA' shows the topography of the mound (image ID: PSP_007570_1415; image center: 38.2°S, 56.2°E). (B) Slope map of the fractured mound and the surrounding terrain. On this map, the red color indicates the high slopes and the green color the low slopes. We can see that the highest slopes are localized at the sides of the mound. (C) Topographic profile A–A' across the fractured mound. The black arrows show where the slope has been measured (15°).*

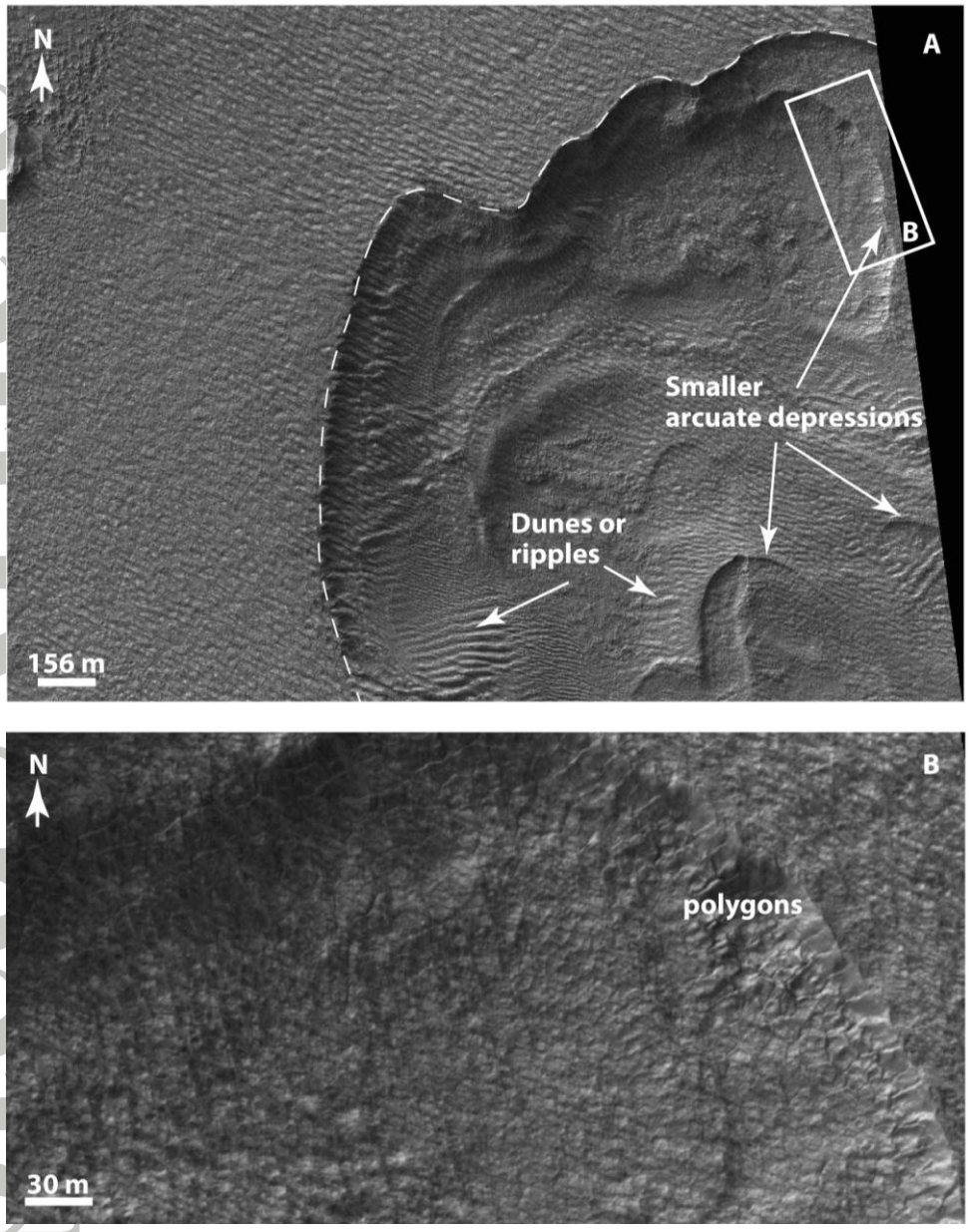

Figure 6. *HiRISE views of large arcuate depressions observed on the surface of a banded terrain. For instance, the encompassing one that has the rim underlined by the white dashed line is ~2 km-wide. (A) Large rimless arcuate depressions displaying in their interior aeolian features like dunes and polygons (image ID: ESP_017565_1400; image center: 39.4°S, 54.6°E). (B) Close-up of the interior of a large arcuate depression indicated by the white box B in Fig. 6A (image ID: ESP_017565_1400; image center: 39.4°S, 54.6°E). This view shows well the multiple polygons observed on the floor of the arcuate depressions.*

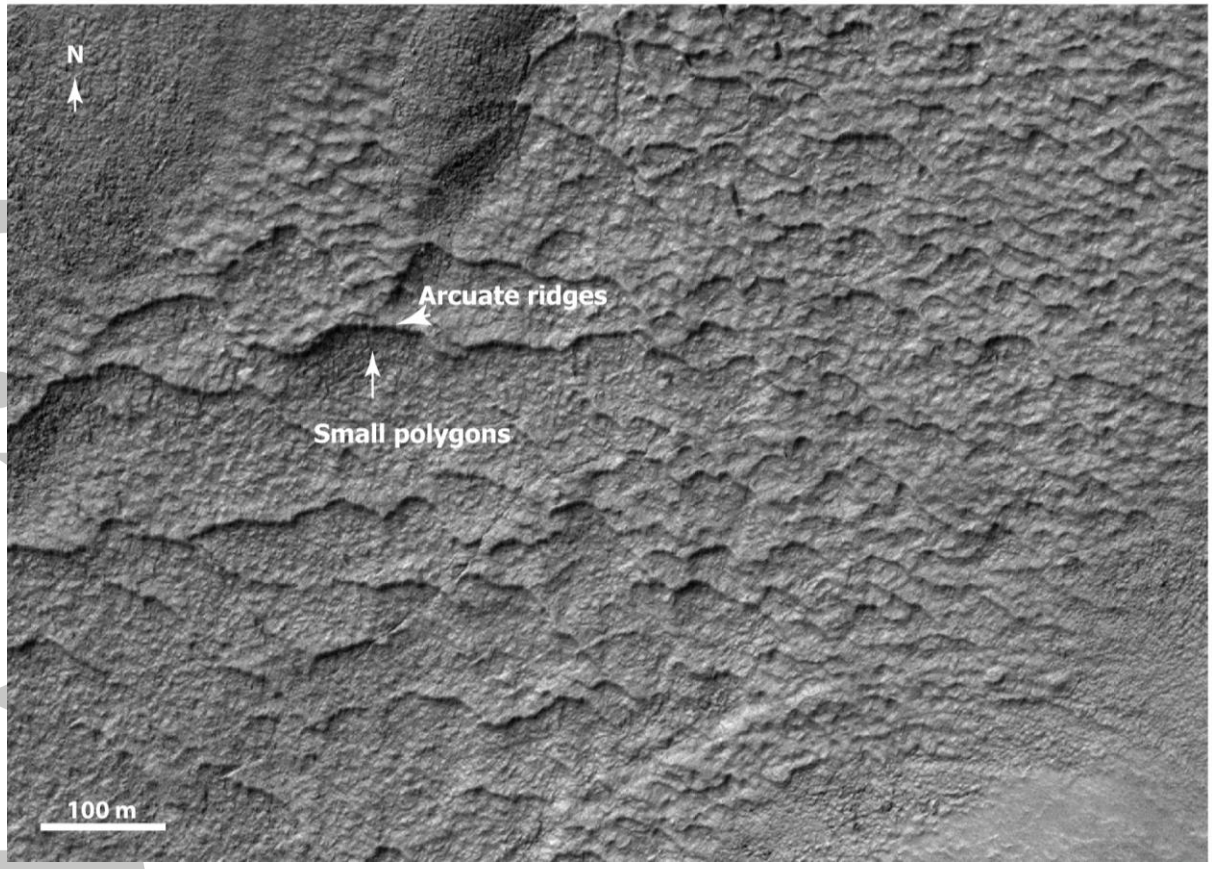

Figure 7. *HiRISE observation showing a field of small arcuate depressions (image ID: ESP_015943_1390, image center: 40.5°S, 54.2°E). This view reveals the arcuate tops of the depressions and the small polygons observable on the floor of the depressions. Here, the arcuate depressions cover a range of different elevations.*

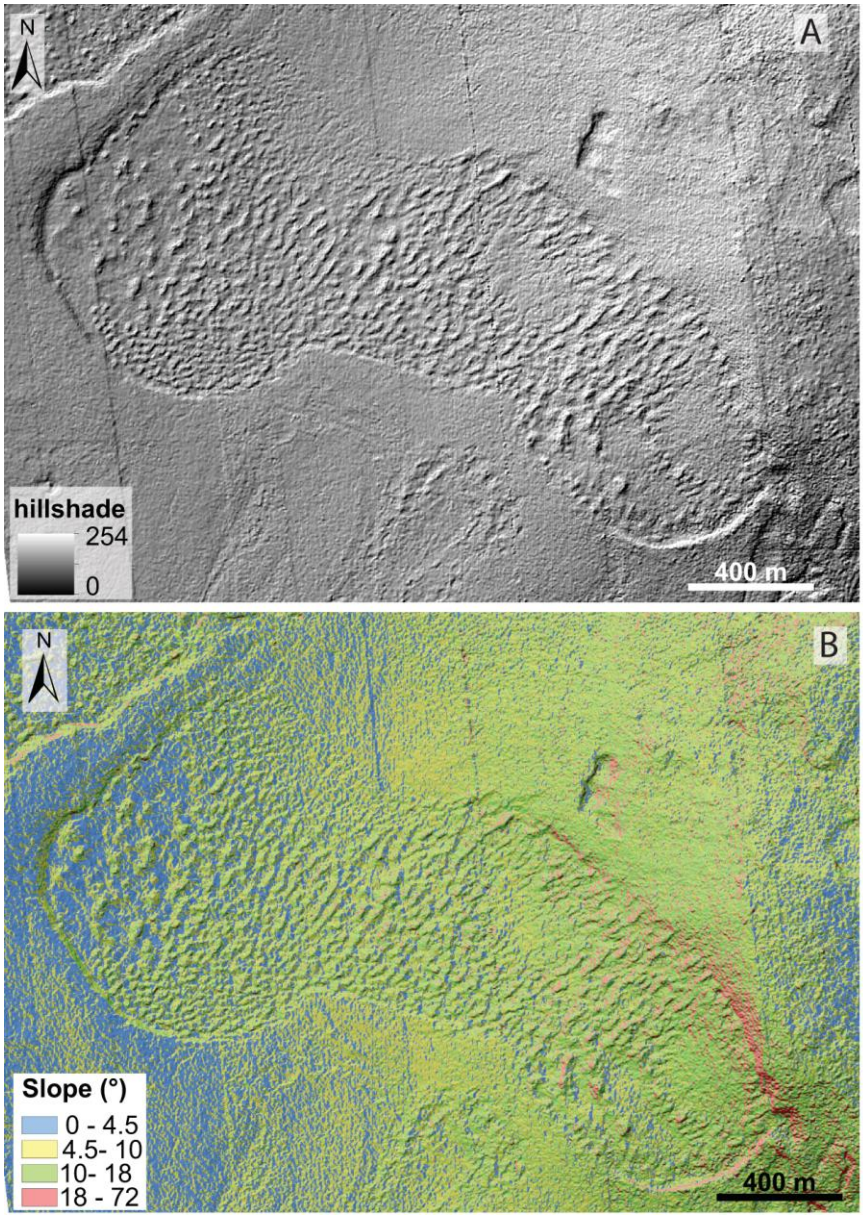

Figure 8. *Hillshade and slope map made from a HiRISE DTM showing a local-scale hummocky area (HiRISE DTM ID: DTEED_007570_1415_006779_1415). (A) This Hillshade shows the multiple blocks constituting the hummocky area. (B) Slope map of the hummocky area and its surrounding surface. The blue color shows the low (0–4.5°) slopes and the red color the high (18–72°) slopes. The sides of the blocks are in green and some are red, indicative of steep slopes between 10 and 20°. The floor between the blocks appears blue, which indicates a relatively gentle slope around 2–4°.*

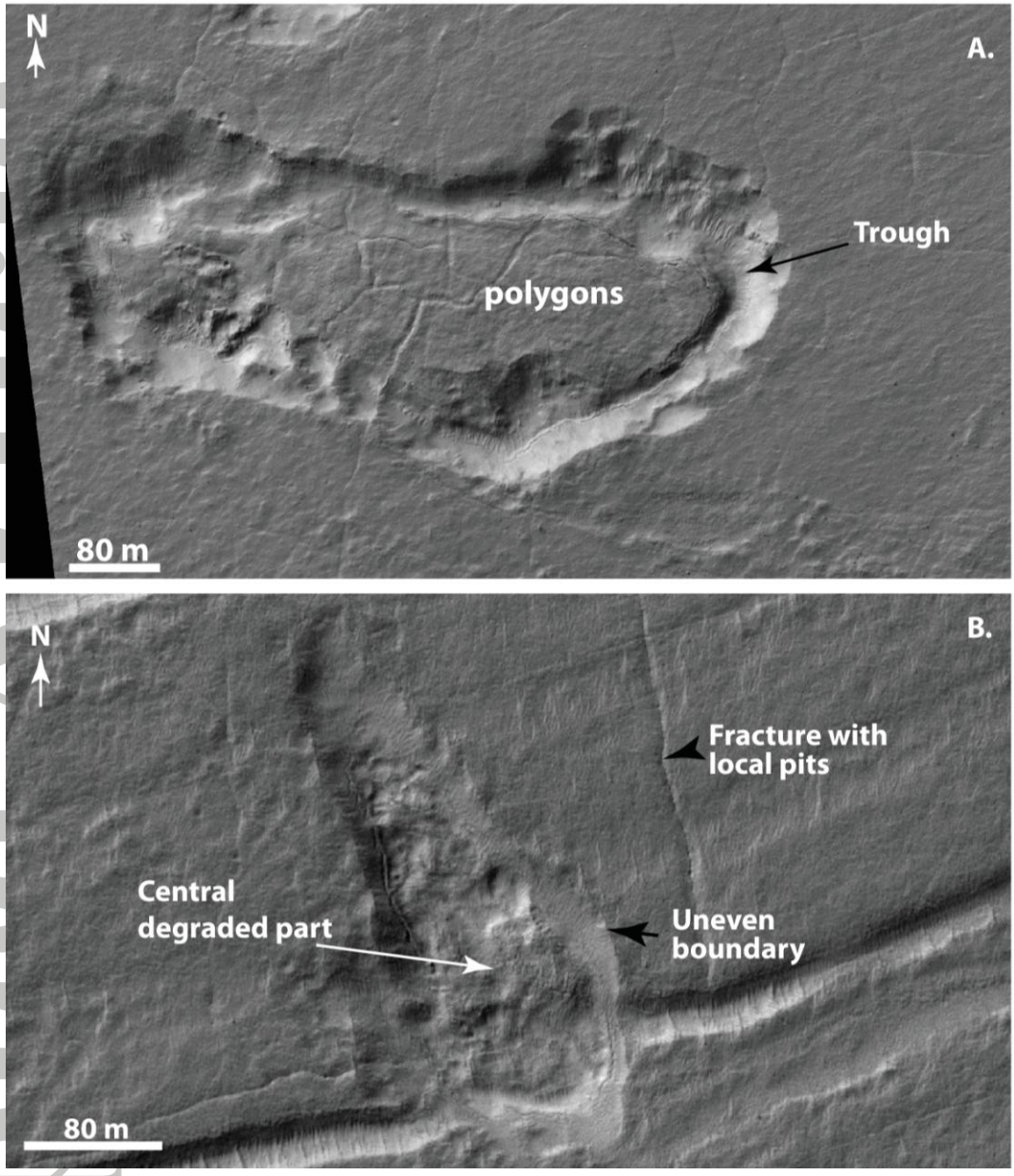

Figure 9. *HiRISE views of both orientations of the elliptical depressions (image ID: PSP_007781_1410, image center: 38.4°S, 55.5°E). (A) Example of elliptical rimless depression oriented E–W. The slightly depressed central part with its top displaying a polygonal pattern of fractures is well visible. (B) Example of elliptical rimless depression oriented N–S. On this HiRISE observation, we can observe the central degraded area surrounded by an uneven sinuous boundary.*

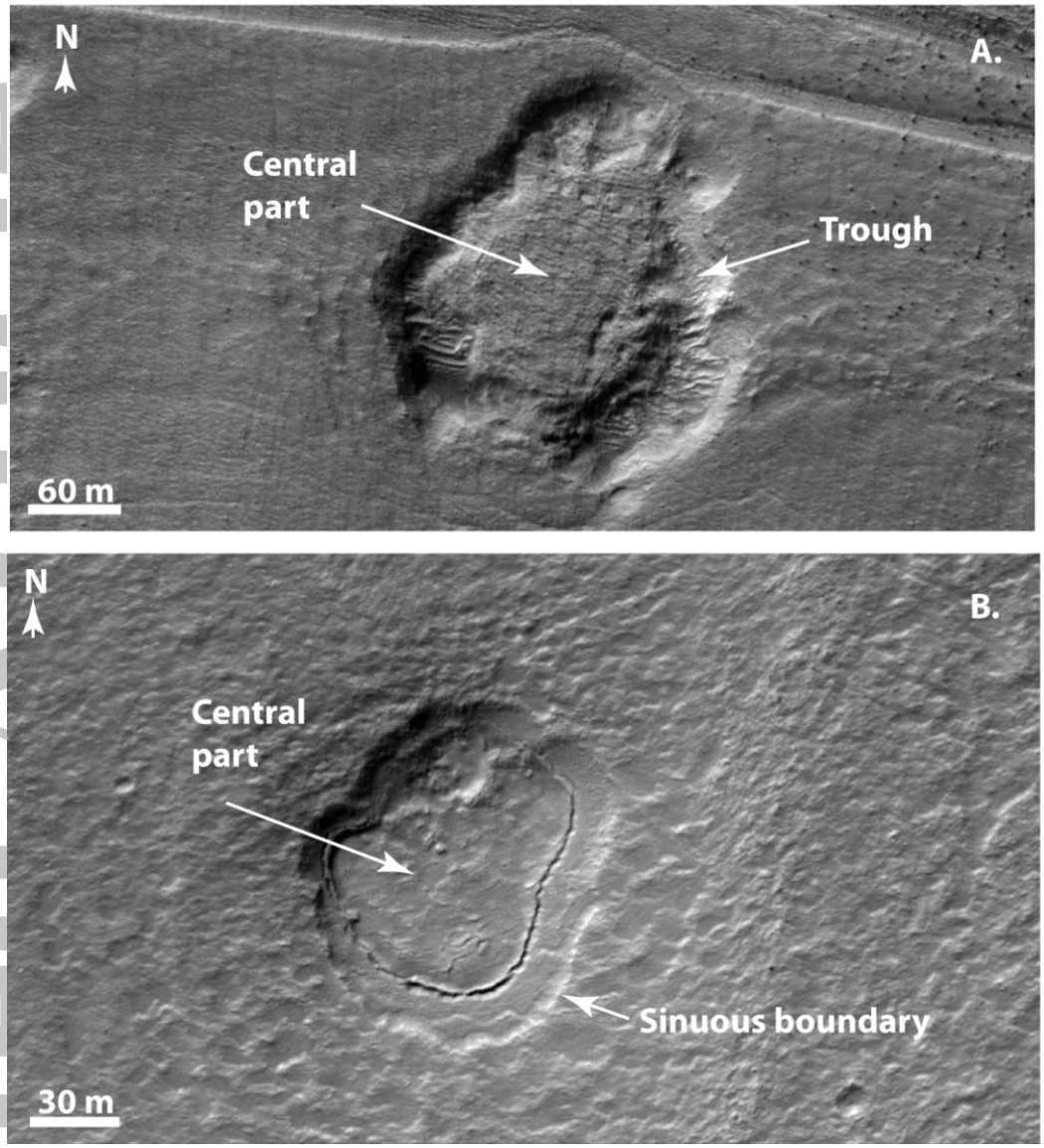

Figure 10. *HiRISE observations of circular depressions. (A) Quasi circular depression with a sinuous trough surrounding a central slightly depressed part (image ID: ESP_026360_1415, image center: 38°S, 57.4°E). (B) Circular rimless depression with its central part surrounded by a sinuous topographic step (image ID: ESP_025635_1395, image center: 40.1°S, 52.2°E)*

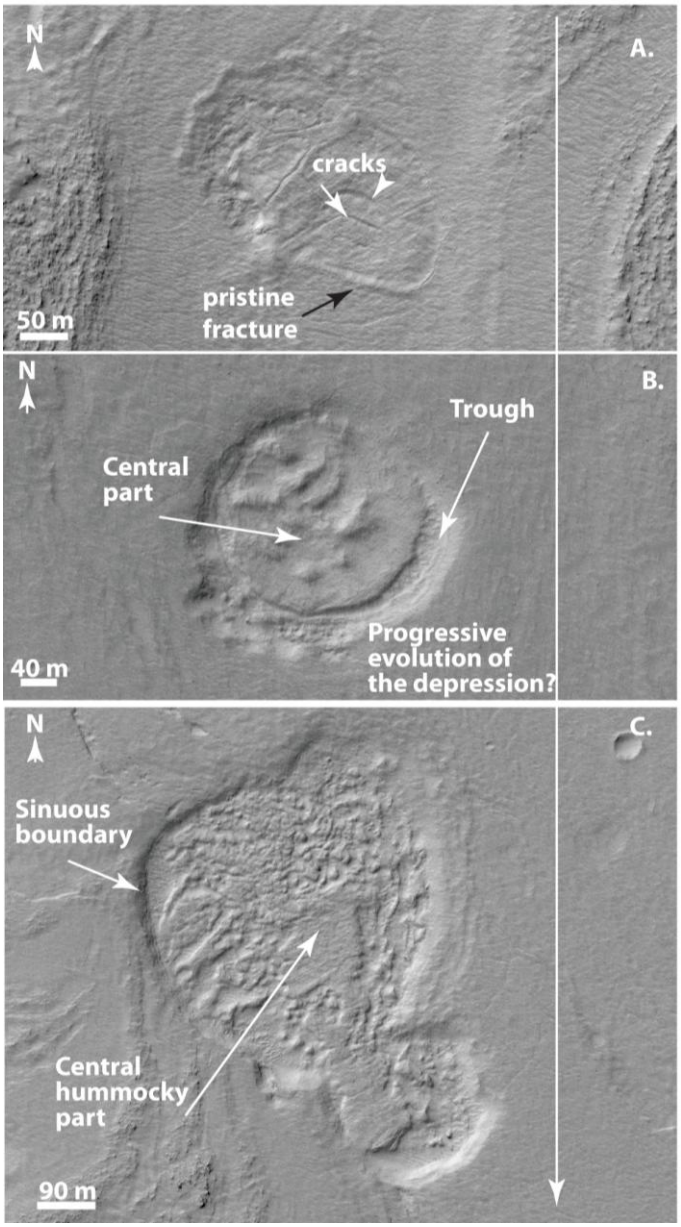

Figure 11. *HiRSE observations that show the progressive evolution of elliptical to circular depressions (image ID: PSP_006568_1415, image center: 38.3°S, 57.4°E). (A) First stage of formation characterized by a pristine circular fracture and a central part at the same topographic level as the surrounding terrains. (B) Intermediate stage of evolution with a well-defined circular trough surrounding a slightly depressed central part. (C) Last stage of evolution with a sinuous boundary and a central part completely degraded to a hummocky pattern.*

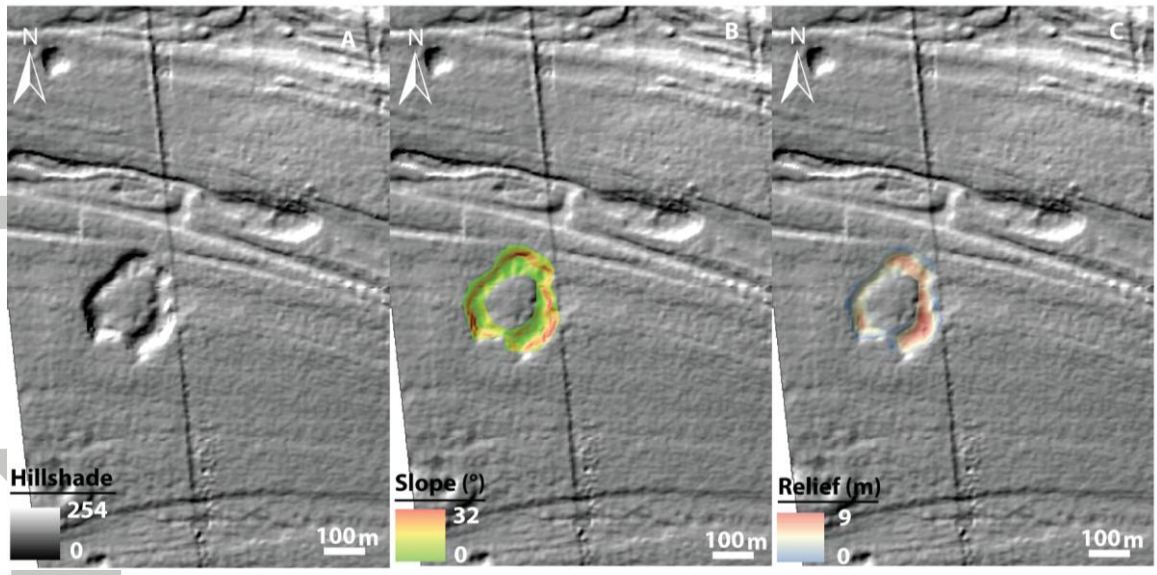

Figure 12. *Example of morphometric analyses of a circular depression made using a HiRISE DTM (DTM ID: DTEED_026360_1415_026426_1415_A01). (A) Hillshade of the relative circular rimless depression. (B) Slope map of the trough surrounding the central part of the structure. Red colors indicate steep slopes for the flanks of the trough and the green color represents the relative flat floor of the trough. (C) Relief map of the trough. The red color indicates the high relief and the blue color the low relief. We can observe that the bottom of the trough appears in red, indicating a high relief.*

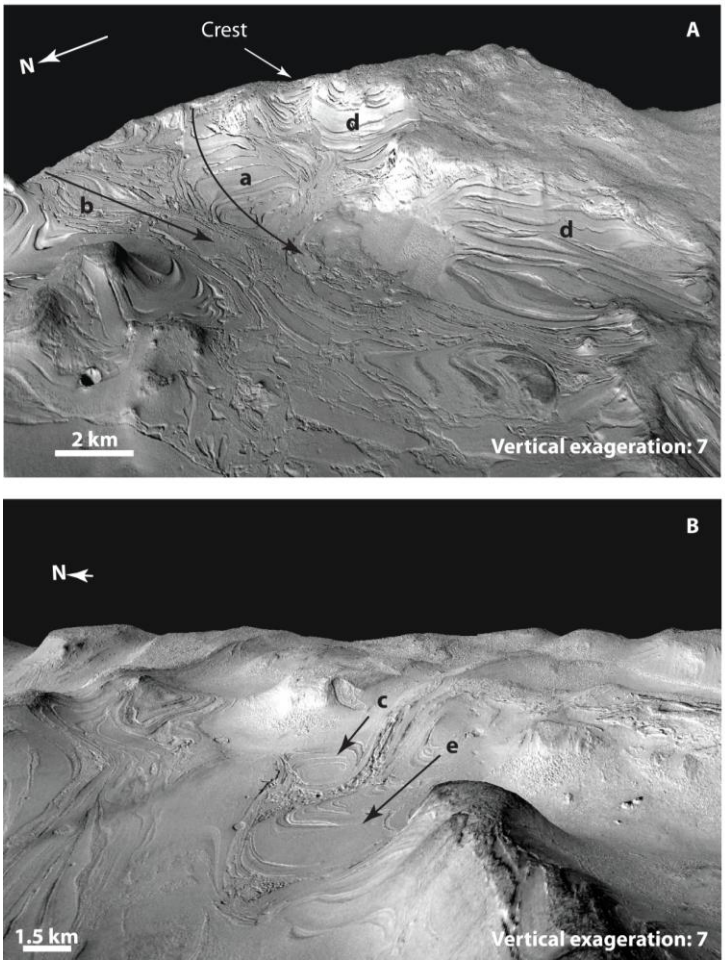

Figure 13. *3D views showing the morphologies of linear and lobate banded terrain controlled by the topography and the neighboring banded terrain. (A) 3D view of a CTX DTM (image pairs B18_016642_1371 – P18_007913_1371) presenting the interaction of a lobate (letter 'a') and a linear (letter 'b') banded terrain. The slight change of direction of the lobate banded terrain 'a' occurred when the lobate banded terrain meets the linear banded terrain 'b'. Curved banded terrain (letters 'd') located on slopes and perpendicular to the direction of the main slope can be observed on this view. The vertical exaggeration of this 3D view is 7. (B) 3D view of a CTX DTM (image pairs G19_025648_1419 – G20_025925_1419) presenting the geometric relationships between a lobate (letter 'e') and a linear (letter 'c') banded terrain. Due to the interaction with the lobate banded terrain 'e', the end of the linear banded terrain is made up of a concentric banded terrain pattern. The vertical exaggeration of this 3D view is 7.*

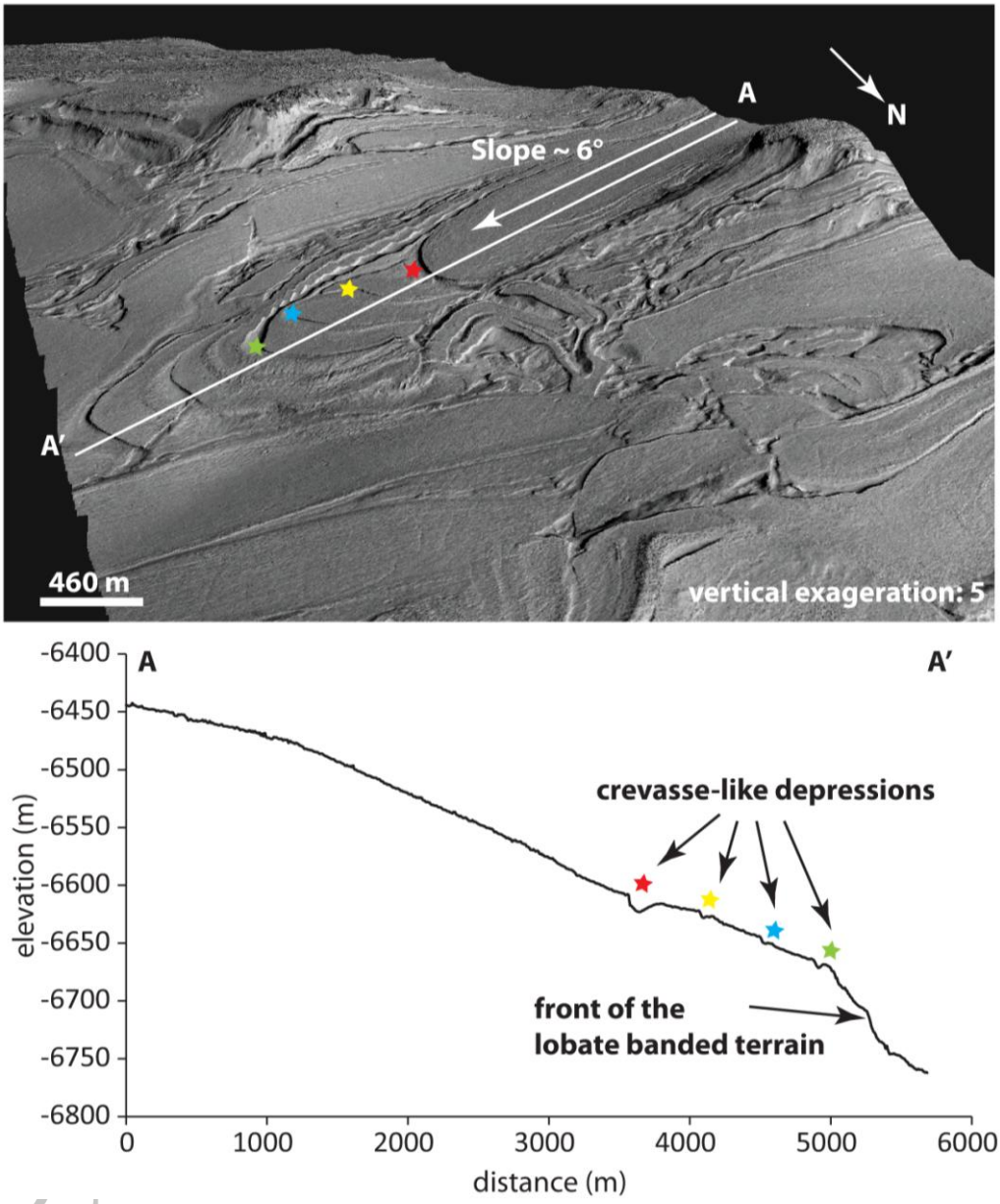

Figure 14. *Morphometric analysis of a unique lobate banded terrain presenting narrow crevasse-like fractures on its surface. (Upper) 3D view of a HiRISE DTM (DTM ID: DTEEC_007491_1405_007201_1405_U01) showing the lobate banded terrain with its associated crevasses-like features (colored stars). The main slope of 6° is indicated by the white arrow and the crevasses-like structures by the colored stars. The white line represents the longitudinal topographic profile (AA'). The vertical exaggeration of the 3D view is 5.*

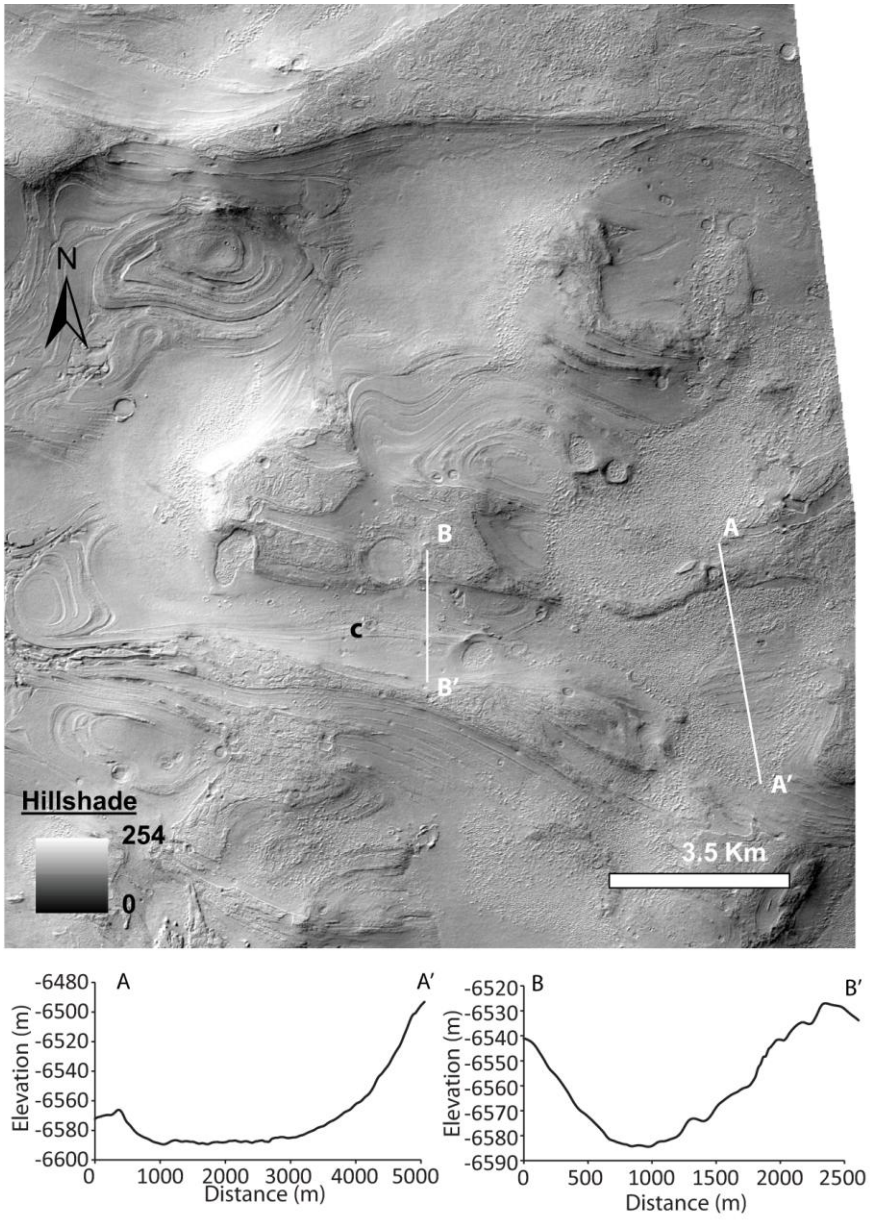

Figure 15. *Hillshade view of the linear banded terrain presented in Fig. 13B with the letter 'c'. (Upper) Hillshade (CTX DTM built from the image pairs G19_025648_1419 – G20_025925_1419) of the linear banded terrain 'c' confined to a well-defined valley. The topographic profiles (AA' and BB') reveal the U-shaped valley.*

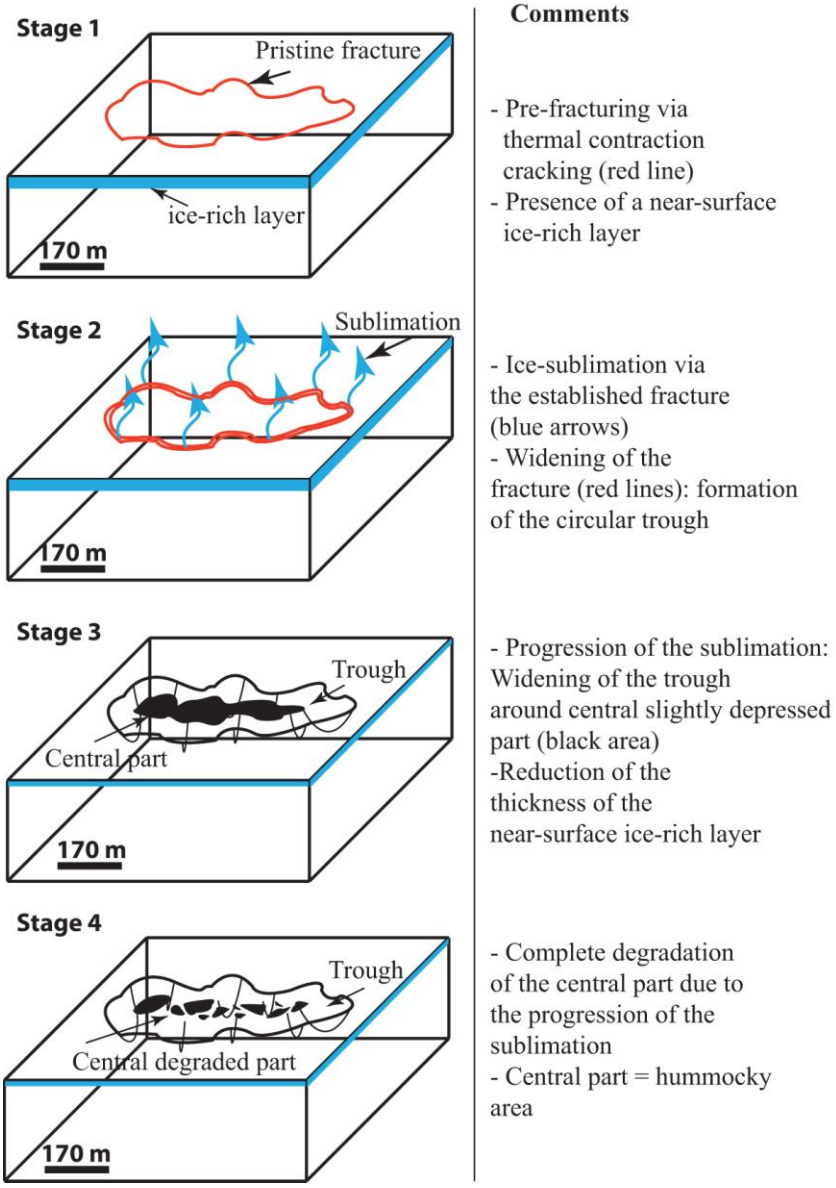

Figure 16. *Sketch of the formation of the elliptical to circular depressions. Stage 1 represents the first step of evolution with the formation of the circular fracture (initial fracture) via thermal contraction cracking. Stage 2 shows the widening of the circular fracture due to sublimation (blue arrows) of the near-surface ice. Stage 3 indicates the presence of a circular trough surrounding the slightly depressed central part. The trough is the result of the degradation of the initial fracture widening with time. Finally, stage 4 consists of the final step of the evolution of the elliptical to circular depressions where the central part is completely degraded to a hummocky area due to the progression of the sublimation.*

Table 1. *Table presenting the HIRISE and CTX DTMs used in this study for the morphometric analysis and the 3D views (type of DTM, DTM IDs or image pairs and spatial resolution).*

Type of DTM	DTM IDs or image pairs	spatial resolution
HiRISE	DTEEC_007491_1405_007201_1405_U01	1 m/pixel
HiRISE	DTEEC_025437_1410_025147_1410_U01	1 m/pixel
HiRISE	DTEEC_007781_1410_008137_1410_U01	1 m/pixel
HiRISE	DTEED_026360_1415_026426_1415_A01	2 m/pixel
HiRISE	DTEED_007570_1415_006779_1415_A01	2 m/pixel
CTX	G19_025648_1419 – G20_025925_1419	20 m/pixel
CTX	B18_016642_1371 – P18_007913_1371	20 m/pixel